



Enhancing cationic superexchange interaction via adjustive lattice distortion in cobalt-based perovskite for improved Fenton-like decontamination

Yijie Wu^a, Tiantian She^a, Yunheng Wang^a, Zhe Xu^{a,*}, Tao Huang^b, Qiuyi Ji^a, Haiou Song^a, Shaogui Yang^a, Shiyin Li^a, Shicheng Yan^b, Limin Zhang^{a,c}, Huan He^{a,*}

^a School of Environment, Jiangsu Engineering Lab of Water and Soil Eco-remediation, Nanjing Normal University, Nanjing, Jiangsu 210023, PR China

^b National Laboratory of Solid State Microstructures, Collaborative Innovation Center of Advanced Microstructures, Eco-Materials and Renewable Energy Research Center (ERERC), College of Engineering and Applied Sciences, Nanjing University, Nanjing, Jiangsu 210093, PR China

^c Green Economy Development Institute, Nanjing University of Finance and Economics, Nanjing 210023, PR China

ARTICLE INFO

Keywords:

Peroxymonosulfate

Perovskite

Lattice distortion

Superexchange interaction

Iohexol

ABSTRACT

The cooperative mechanism of mixed transition metals (TMs) for heterogeneous peroxymonosulfate (PMS) based water treatment can be considered in the viewpoint of cationic superexchange interaction. Herein, Co-Fe cooperation towards PMS activation was studied by modulating octahedral TMO₆ units in Fe-substituted LaCo_{1-x}Fe_xO₃ perovskites. Certain lattice distortion formed at these reactive centers due to Co-Fe ionic radii mismatch, while LaCo_{0.95}Fe_{0.05}O₃/PMS (0.136 min⁻¹) achieved superior performance for iohexol degradation. Cobalt cations are identified as active sites by targeted poison and spectroscopic measurements, which prefer to accept electrons from Fe ions. Experimental and theoretical investigations illustrate that slight Fe-substitution induced lattice distortion leads to Co-O-Fe superexchange interaction, facilitating interfacial electron transfer and cationic valence exchange. And, the tolerance factor of catalysts is also indicated as an indicative descriptor to evaluate structure-dependent performance. Our work attempts to shed light on dual TM interactions for synergistic catalysis towards efficient Fenton-like decontamination.

1. Introduction

Peroxymonosulfate(PMS)-based oxidation is one of attractive advanced oxidation processes to remove refractory contaminant for clean water in recent years [1,2]. This Fenton-like technique provides reactive oxygen species (ROS) with highly oxidative capability of 1.8 ~ 3.1 V vs. NHE, which involve sulfate radical (SO₄^{•-}), hydroxyl radical (•OH), superoxide radical (O₂^{•-}) and non-radical singlet oxygen (¹O₂) [3,4]. Many activating strategies are explored to break the superoxide bond (O-O) of HO-O-SO₃⁻ in PMS to spark these chain reactions, because its high cleavage energy (140 ~ 213.3 kJ mol⁻¹) usually impedes the ROS generation [5]. Heterogeneous transition metal activation is a promising method to minimize energy consumption and secondary metal contamination, especially the cobalt-based oxides presenting superior activity than other 3d transition metals (TMs) [6,7]. However, the Co redox pairs still suffer from sluggish interaction with PMS (Co²⁺ + HSO₅⁻ → Co³⁺ + SO₄^{•-} + OH⁻, Co³⁺ + HSO₅⁻ → Co²⁺ + SO₅^{•-} + H⁺) [8]. Apart

from the cationic morphological regulation and single-atom construction, the TM-O₆ octahedron in oxides is recently considered as the fundamental unit for catalytic activity [9,10]. The cobalt-based perovskites thus are gaining immense attentions, because they can afford excellent platforms to construct various typical octahedral sites for deep investigation on PMS activation [11].

The ABO₃-type perovskite has emerged as a model candidate to activate peroxide for contaminant degradation, where A site is occupied by a rare-earth or alkaline-earth group metal and B site is filled with transition metals. Its cubic phase can be regarded as B-O₆ octahedron surrounded with A cations, and the physiochemical properties and electronic structures can be tailored by modulation of A-, B- and/or O-sites. The A position is usually responsible for stabilizing the perovskite structure, and the lanthanide (La) cation is widely employed at A site among diverse ACoO₃ (A = La, Ba, Sr, Ce) [12], owing to its feasible exposure of active sites and superior catalytic activity for PMS activation towards organic degradation [13]. On the other hand, the cobalt (Co) is

* Corresponding authors

E-mail addresses: zhexu@njnu.edu.cn (Z. Xu), huanhe@njnu.edu.cn (H. He).

<https://doi.org/10.1016/j.apcatb.2023.123569>

Received 15 September 2023; Received in revised form 21 November 2023; Accepted 25 November 2023

Available online 28 November 2023

0926-3373/© 2023 Elsevier B.V. All rights reserved.

extensively utilized at B position [14], because Co always presents great activity for persulfate-based oxidation among multiple LaBO_3 (B = Cu, Fe, Mn, Co and Ni etc.) perovskites [15]. Furthermore, the excessive La/Co deficiency and substitution of oxygen by foreign ions (e.g. boron and halogen anions) are also built to promote PMS activation [16–19]. These regulations on A-, B- and/or O- ions are considered to form non-stoichiometric perovskites, especially generating oxygen defects. This transformation is regarded as the reason of improved catalytic performance in most reports. The oxygen vacancy (V_O) and filled oxygen (O_f) have been inferred as direct sites to react with HSO_5^- via capturing and releasing oxygen in PMS [20,21]. In contrast, the targeting poisoning and theoretical calculation also suggest oxygen defects work mainly for indirect reaction, which promote the PMS adsorption, electron transfer and valence change of TM cations [22,23]. The catalyst could present excellent stability even the amount of V_O decreases after reuse [24]. Therefore, these mechanistic debates indicate the functions of B-site cation need further study, as the perovskite-based PMS activation is primarily subjected to d-band center heterogeneous catalysis [25].

The modulation of mixed TMs with cobalt at B position has a profound impact on catalytic performance comparing to single metal ones [21], which governs main electron exchanges between perovskites and reactants. The partial substitution of Co by Cu acquires elevated contaminant degradation on $\text{LaCo}_{0.4}\text{Cu}_{0.6}\text{O}_3$ [26], and the induced Mn could tune the electron filling on Co e_g-orbital to obtain a series of $\text{LaCo}_{1-x}\text{Mn}_x\text{O}_{3+\delta}$ ($x = 0, 0.3, 0.5, 0.7$, and 1.0) perovskites and respective performances [27]. And, the increased Co/Mn ratio in shape-controlled $\text{La}_{0.5}\text{Ba}_{0.5}\text{Co}_x\text{Mn}_{1-x}\text{O}_{3-\delta}$ results in more low-valence Co^{2+} cations to generate $\text{SO}_4^{\cdot-}$ [28]. Furthermore, iron is also an important participant in peroxide activation. Apart from regulating the ratio of Co/Fe [29], the SiO_2 membrane [30] and Ti_4O_7 substrate [31] have been employed to optimize the synergetic effect of Fe and Co for PMS activation. However, the optimal replacement amount of Fe presents a huge difference from $\text{LaCo}_{0.1}\text{Fe}_{0.9}\text{O}_3$ to $\text{LaCo}_{0.75}\text{Fe}_{0.25}\text{O}_3$ [32,33], and the primary ROS is also uncertain among sulfate radicals and non-radical $^1\text{O}_2$. Though oxygen species (vacancies, lattice oxygen, and interstitial oxygen) are also considered to affect catalytic activity in these $\text{LaCo}_{1-x}\text{Fe}_x\text{O}_{3-\delta}$ /PMS systems, the mechanisms of mixed B-site cations on forming oxygen defects and decomposing PMS remain finite understanding except non-stoichiometric effect. It is worthy considering that superexchange interactions exist in crystal lattice via the corner sharing tetrahedra/octahedra and edge-sharing octahedra/octahedra arrangements. Since $\text{LaCo}_{1-x}\text{Fe}_x\text{O}_3$ has abundant corner sharing TMO_6 units, the superexchange between TM cations arise through oxygen anion (e.g., Co–O–Co, Co–O–Fe), instead of direct TM–TM interaction via t_{2g} orbital overlap [34]. Even perovskite platform offers great structure flexibility, the B-site cationic substitution still gives rise to lattice distortion inevitably. The relational distortions would have certain modulation on crystalline and electronic properties of perovskites [35–37], affecting TM superexchanges. Therefore, mechanistic insight on mixed TM sites in perovskites for PMS activation still demands further studies.

Herein, a family of perovskite $\text{LaCo}_{1-x}\text{Fe}_x\text{O}_3$ ($x = 0, 0.05, 0.1, 0.2, 0.5, 0.8, 0.99, 1$) were synthesized to study the synergetic effect of B-site TMs by modulating the lattice distortion, using the moderate radius difference of octahedral cations. The typical iodinated contrast media i. e. iohexol (IOH) was chosen as target contaminant, which is massively employed for myelography and computerized tomography, companying with the environmental risk to become toxic disinfection by-products (DBPs) during water disinfection. Systemic performances of IOH removal were measured to reflect the intrinsic PMS activation on perovskites. ROS were determined via quenching experiments to study the mechanism of PMS decomposition. Spectroscopic and electrochemical measurements were adopted to survey chemical states on reactive centers and relational electron transfer with PMS. Theoretical calculation was operated to reveal the changed electronic structure of perovskites depending on Co-Fe synergism. Besides, the IOH degradation pathways

and main toxicity analysis were performed to further evaluate PMS activation. Our work attempts to understand cooperative electronic interaction of octahedral TMs in PMS activation for designing rational perovskite-type for efficient water treatment.

2. Experimental section

2.1. Chemical reagents

All chemicals were of analytical reagent (AR), and purchased for direct use without further purification. The La, Fe and Co based hydrated nitrates and citric acid were obtained from Sinopharm Chemical Reagent Co., Ltd. The commercial potassium PMS (Oxone, $2\text{KHSO}_5 \cdot \text{KHSO}_4 \cdot \text{K}_2\text{SO}_4$) and iohexol (IOH) were acquired from Aladdin Reagent. The spin-trapping agents, e. g. 5,5-dimethyl-1-pyrrolidine N-oxide (DMPO) and 2,2,6,6-tetramethyl-4-piperidone (TEMP) were procured from Sigma-Aldrich. Other chemicals and reagents are presented in Text S1.

2.2. Catalyst synthesization

The classical sol-gel method was carried out to synthesize cobalt-iron perovskite $\text{LaCo}_{1-x}\text{Fe}_x\text{O}_3$ ($x = 0, 0.05, 0.1, 0.2, 0.5, 0.8, 0.99, 1$), where the different stoichiometric ratios of cations were obtained by changing the corresponding metal amount of La, Fe and Co nitrates. The mixing sol with citric acid solution were heated for ageing to obtain the gel, which were then dried and calcined at high temperature to obtain the desired materials. The detailed preparing processes are described in Text S2.

2.3. Characterization

The phase structures of as-prepared samples were determined by powder X-ray diffraction (XRD). The morphologies of the products were measured by a scanning electron microscope SEM. X-ray photoelectron spectroscopy (XPS) was performed to survey chemical states. Spin-trapping signals detecting (non) radical intermediates were collected by continuous-wave X-band electron paramagnetic resonance (EPR). The detailed characteristic methods were depicted in Text S3.

2.4. Catalytic degradation performance

The catalytic performance of iron-cobalt perovskite was evaluated for PMS activation and IOH degradation. All reactions are carried out at room temperature. A pseudo first-order kinetic model was adopted for the estimation of observed reaction rate constants, following the equation $k_{\text{obs}} = -\ln(C_t/C_0)$. More information about activity evaluation was presented in Text S4.

2.5. Electrochemical characterization

The electrochemical measurements were performed in a three-electrode cell using an electrochemical analyzer (CHI 760E, Shanghai Chenhua, China) and rotating disk electrode (RRDE-3A, ALS Co., Japan). Perovskite catalysts loaded on glassy carbon electrode served as a working electrode with the loading density of about 0.5 mg cm^{-2} . And, a Pt foil and saturated calomel electrode (SCE) were applied as a counter and reference electrode, respectively. All potentials discussed in this work refer to the reversible hydrogen electrode (RHE) potential. Detailed electrochemical tests were presented in Text S5.

2.6. Theoretical calculation

All the calculations are performed in the framework of the density functional theory with the projector augmented plane-wave method [38], as implemented in the Vienna ab initio simulation package [39].

The generalized gradient approximation proposed by Perdew, Burke, and Ernzerhof is selected for the exchange-correlation potential [40]. The cut-off energy for plane wave is set to 500 eV. The energy criterion is set to 10^{-5} eV in iterative solution of the Kohn-Sham equation. The Brillouin zone integration is performed using $4 \times 4 \times 4$ and $2 \times 2 \times 4$ k-meshes for pure and Fe-doped LaCoO_3 . All the structures are relaxed until the residual forces on the atoms have declined to less than 0.05 eV/Å. The on-site Coulomb interactions for the localized *d* orbitals are parametrized by $U_{\text{eff}} = U - J$ using the PBE functional, and the U_{eff} for Fe, Co, La were set to be 5.3, 3.32, 6.0 eV [41,42]. Detailed calculations were described in Text S6.

3. Results and discussion

3.1. Characteristics of cobalt - iron perovskite catalysts

As schemed in Fig. 1a, the octahedral TMO_6 units belong to the corner sharing arrangements in perovskites, which is different from the edge-sharing octahedra/octahedral connections in spinel catalysts [43]. It means that the electronic structures of octahedral centers in $\text{LaCo}_{1-x}\text{Fe}_x\text{O}_3$ would be sensitive to the crystal strain, which plays an important role on the electron distribution and transfer. Octahedral cobalt ions prefer to remain low-spin state [44], so the 3d orbital electrons are localized for poor electron transfer. The substitution of heteroatom was supposed to adjust the electronic structure. The phase structures of as-prepared $\text{LaCo}_{1-x}\text{Fe}_x\text{O}_3$ with various Co/Fe atomic ratio were determined by XRD patterns shown in Fig. 1b. The characteristic diffraction peaks of LaCoO_3 (JCPDS No. 75-0279) and LaFeO_3 (JCPDS No. 75-0541) are observed in the range of $20^\circ \sim 60^\circ$, respectively. The similar diffraction peaks suggest cubic perovskites with space group of Pm-3m are achieved. These samples emerge high purity, because no abrupt peaks appear at any other diffraction angle. The highest peak of LaCoO_3 having no Fe doping is located at 33.14° , which is assigned to the (110) plane. With the substitution of Fe increased, this specific peak

is shifted left gradually. And, the ICP analysis in Table S1 confirms that Co/Fe ratios comply with the precursor proportion owing to the well flexibility of chemical composition in perovskites. The corresponding diffraction angle is finally decreased to about 32.52° for LaFeO_3 when Co cations was completely replaced by Fe cations, owing to the larger ion radius of Fe ion (0.78 Å) than Co ion (0.75 Å) [45]. It is worth noting that the change of (110) peak position indicates the occurrence of lattice distortion in mixed $\text{LaCo}_{1-x}\text{Fe}_x\text{O}_3$ perovskite catalysts.

The structure and bonding composition of these $\text{LaCo}_{1-x}\text{Fe}_x\text{O}_3$ were further inspected by Fourier transform infrared spectroscopy (FTIR) spectra displayed in Fig. 1c. The broad bands at about 560 and 600 cm^{-1} could be associated with B-O stretching vibration of octahedral TMO_6 units, because the B-site cation generally has six coordination with oxygen anions to form octahedrons in ABO_3 -type perovskite structures [46]. Meanwhile, the adsorption peak at the lower wavenumber of 560 cm^{-1} is attributed to octahedral Fe-O stretching vibration [47]. In addition, the peaks observed between about 900–1750 cm^{-1} are given rise to the TM-O vibrations in perovskites [48]. The related stretching peaks of TM-O bonds in other $\text{LaCo}_{1-x}\text{Fe}_x\text{O}_3$ perovskites exhibit medium wavenumbers between and LaCoO_3 and LaFeO_3 . The FT-IR results are in good line with XRD measurements, which further confirms the lattice distortion could be modulated by different Fe substitution in $\text{LaCo}_{1-x}\text{Fe}_x\text{O}_3$ perovskites.

3.2. Removal performance of IOH on $\text{LaCo}_{1-x}\text{Fe}_x\text{O}_3$ via PMS activation

The catalytic activity of these TM-mixed $\text{LaCo}_{1-x}\text{Fe}_x\text{O}_3$ perovskites towards PMS activation can be reflected by removing target contaminant IOH. The degrading performances of the synthesized catalysts with different Co/Fe ratios are shown in Fig. 2a, where the measurement at each condition was performed at least three times to ensure its reliability. LaCoO_3 could completely remove IOH within 30 min, while LaFeO_3 exhibited little capability to degrade contaminant. And, the $\text{LaCo}_{0.01}\text{Fe}_{0.99}\text{O}_3$, $\text{LaCo}_{0.2}\text{Fe}_{0.8}\text{O}_3$ and $\text{LaCo}_{0.5}\text{Fe}_{0.5}\text{O}_3$ also could not

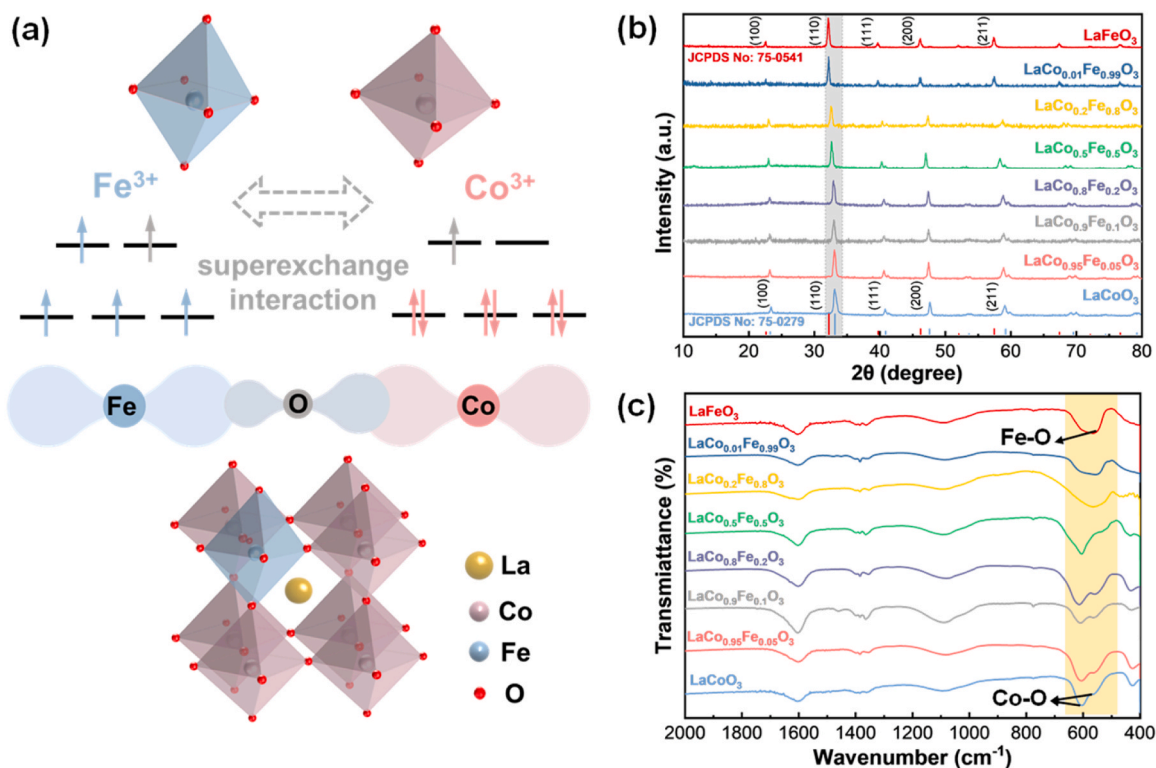


Fig. 1. The crystalline structures (a), XRD patterns (b) and FTIR spectra (c) of $\text{LaCo}_{1-x}\text{Fe}_x\text{O}_3$ ($x = 0, 0.05, 0.1, 0.2, 0.5, 0.8, 0.99$) perovskites with various Fe substituted ratio at B sites.

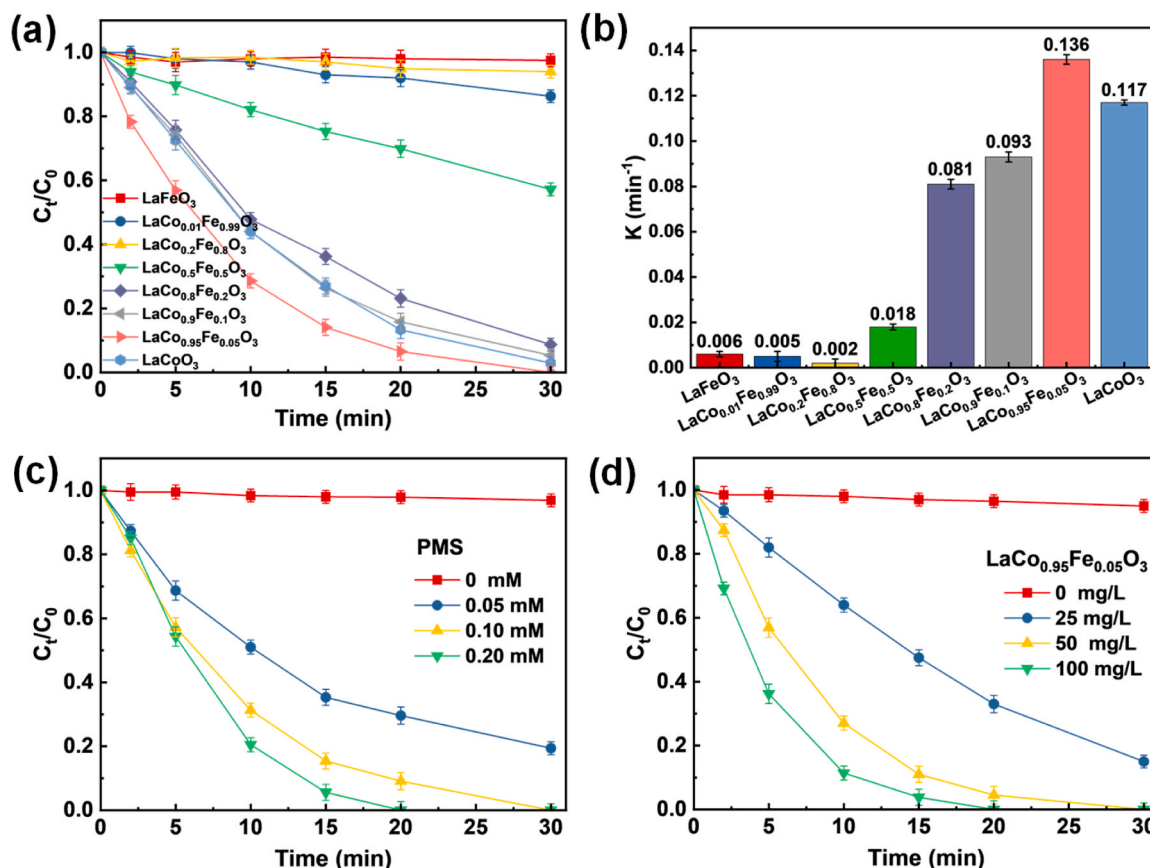


Fig. 2. Performances (a) and correlated k_{obs} (b) of IOH degradation on LaCo_{1-x}Fe_xO₃ catalysts via PMS activation, effect of different PMS dosages (c) and catalyst dosages (d) on contaminant removal of the LaCo_{0.95}Fe_{0.05}O₃/PMS system. Reaction conditions: [catalysts] = 0 ~ 100 mg L⁻¹, [PMS] = 0 ~ 0.2 mM, [IOH concentration] = 10 mg L⁻¹.

reach 50 % removal efficiency in half an hour. In contrast, LaCo_{0.9}Fe_{0.1}O₃ and LaCo_{0.8}Fe_{0.2}O₃ achieved more than 90 % of IOH removal in the same reaction period, even the degradation effect was still inferior to that of LaCoO₃. These performances suggest that LaCo_{1-x}Fe_xO₃ has little activity to activate PMS when the substituting ratio of Fe is over 50 %. It is interesting that LaCo_{0.95}Fe_{0.05}O₃ presents superior performance even than LaCoO₃, which could nearly remove 50 % IOH in the first 5 min. Then, the observed reaction rate constants (k_{obs}) are calculated by fitting the degradation reactions following the quasi first-order kinetic. As shown in Fig. 2b, over half substitution of iron cations leads to negligible rate constant, due to the intrinsic poor activity of iron-based PMS activity. With the ionic rate of Fe decreased, the reaction rate of LaCo_{0.8}Fe_{0.2}O₃ and LaCo_{0.9}Fe_{0.1}O₃ obviously increased to 0.081 and 0.093 min⁻¹, respectively. And, the reaction rate of the LaCoO₃ sample was even less than 80 % of that of LaCo_{0.95}Fe_{0.05}O₃ sample. The just 0.5 % Fe substitution contributes to superior k_{obs} value of 0.136 min⁻¹ comparing to LaCoO₃ (0.117 min⁻¹), which is nearly 26 times higher than those of Fe host perovskites. Similar to positive effects in water oxidation, the participation of trace Fe contributes to promote peroxide oxidation.

To evaluate the cooperation of mixed TM cations on PMS activation effectively, conventional dosages of catalyst and PMS were screened. The used amount of PMS would affect the final percentage of residual IOH shown in Fig. 2c. The absence of PMS hardly leads to IOH degradation. The target contaminant could be degraded by 70 % when 0.05 mM PMS is applied, and the complete removal would be realized with PMS concentration over 0.1 mM. It means that too little PMS cannot support effective IOH degradation while too much PMS will bring unnecessary reactant waste. Thus, the moderate PMS concentration of 0.1 mM was used for following investigation. Based on the

similar principle, the condition of catalyst was chosen as 50 mg L⁻¹ according to the results in Fig. 2d. In heterogeneous PMS activation, the catalyst surface provides active sites to decompose peroxide, and the ROS generated from adsorbed PMS probably further interact with catalyst and/or adjacent species. It indicates that the overdose of PMS or perovskites would generate too many active species, and lead to complicated interaction among various ROS disturbing the intermediates observation. Therefore, the moderate reactant dosages were selected to provide a rather mild heterogeneous environment.

3.3. Effects of lattice distortion

Companing with LaCoO₃ and LaFeO₃, the superior LaCo_{0.95}Fe_{0.05}O₃ was selected as the typical proportional sample for focused structure and spectroscopy analysis. The ICP test listed in Table S1 shows that the ratio of Co to Fe in LaCo_{0.95}Fe_{0.05}O₃ is close to 95:5, which indicates that the mixed B-site TMs in the synthesized material is in accordance with expectations. Then, the morphologies of perovskites are observed by SEM images in Fig. 3a-c. LaCoO₃ and LaFeO₃ reveal similar network structure resulted from crystalline collapse during high temperature calcination. The LaFeO₃ emerges a rougher surface than LaCoO₃, as the Fe replacement gives rise to enhanced deviation from ideal perovskite structure. Meanwhile, the sol-gel process provided LaCo_{0.95}Fe_{0.05}O₃ the feature of cross-linked framework, which probably brings about abundant surface area for the adsorption of contaminant and active species. This hypothesis will be examined by ROS capture and interface characteristics below.

Moreover, TEM was performed to observe microscopic bulk and interface features. As presented in Fig. 3d-f, all the network perovskites are made up of nanoparticles, whose diameter are around 20 ~ 100 nm.

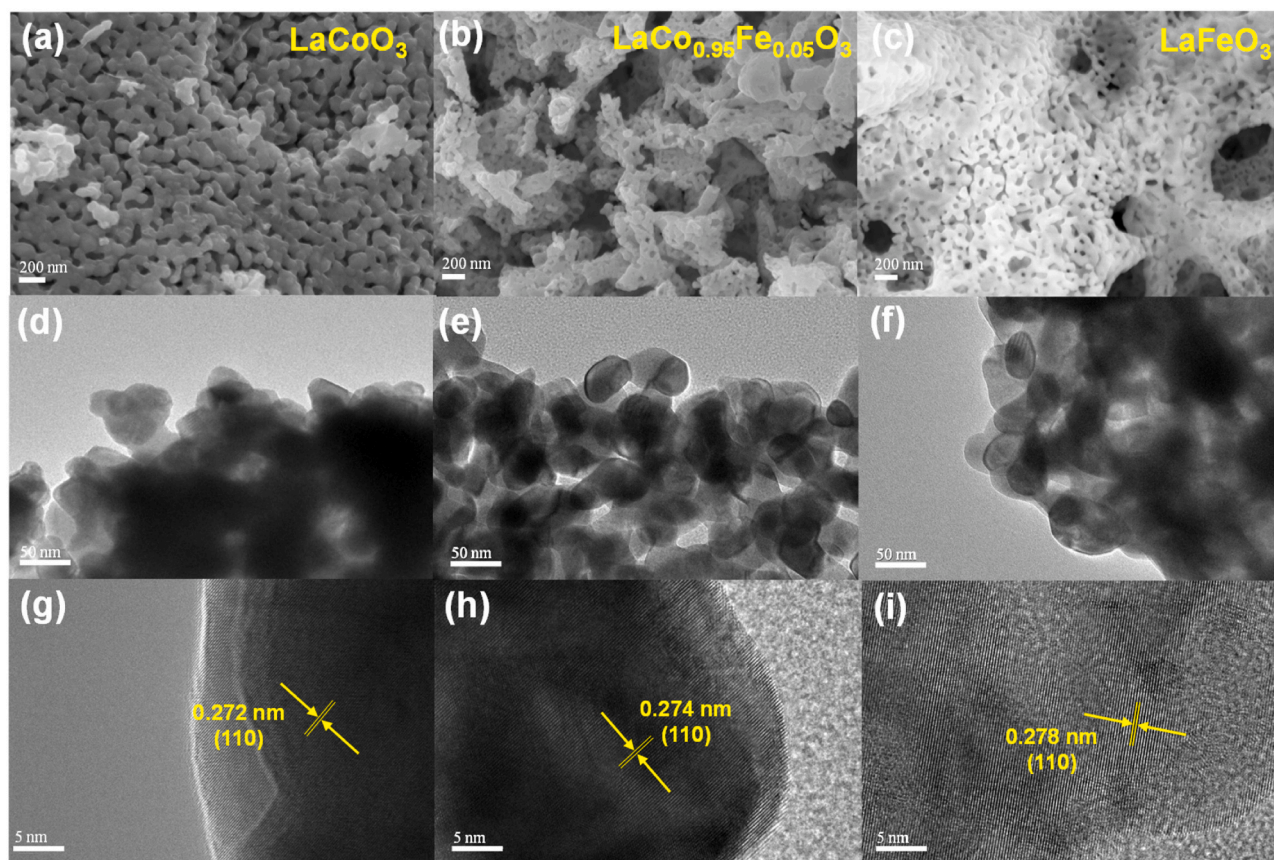


Fig. 3. Morphological images of SEM, TEM and high-resolution TEM (HR-TEM) of LaCoO_3 (a, d, g), $\text{LaCo}_{0.95}\text{Fe}_{0.05}\text{O}_3$ (b, e, h) and LaFeO_3 (c, f, i).

The high-resolution TEM images collected in Fig. 3g-i provide a precise insight to crystalline structure. The main lattice distance of 0.272, 0.274 and 0.278 nm are observed in LaCoO_3 , $\text{LaCo}_{0.95}\text{Fe}_{0.05}\text{O}_3$ and LaFeO_3 , respectively. The increase of interplanar spacing with Fe substitution is consistent with the left shift of related peak in XRD patterns in Fig. 1b. In addition, the selected area electron diffraction (SAED) of $\text{LaCo}_{0.95}\text{Fe}_{0.05}\text{O}_3$ exhibits the polycrystalline feature in Fig. S1, which also illustrates the (100), (110) and (111) crystalline planes corresponding to the XRD peaks. These slightly different lattice fringes are ascribed to the stressed (110) facets in perovskites, further confirming the lattice distortion adjusted by the radii mismatch of cobalt and iron cations.

As depicted in Fig. 4a, the asymmetric signals at the g factor of 2.003 are originated from the existence of oxygen defects [49]. $\text{LaCo}_{0.95}\text{Fe}_{0.05}\text{O}_3$ presents the strongest V_O signal, which is probably attributed to plentiful structural defects accompanied by the bulk lattice distortion. It is worth noting that LaCoO_3 exhibits a higher catalytic activity than LaFeO_3 , though the former processes weaker V_O intensity than the latter. In addition, the tolerance factor (t factor) can be employed to further understand the structure-activity relationship. It is because that the t factor is an effective descriptor to evaluate perovskite structure, following the formula i.e. $t = \frac{R_A + R_O}{\sqrt{2}(R_B + R_O)}$, where R_A , R_B and R_O are the ionic radii of A-site, B-site and O-site ions [50]. The ideal cubic perovskite is formed at the t value from 0.9 to 1.1. The t factor of LaCoO_3 (0.971) is closer to 1 comparing with LaFeO_3 (0.954), which might restrain the oxygen deficiency. It also suggests that the large V_O concentration does not positively lead to great performance in this perovskite/PMS system.

XPS measurements were further applied to determine surface chemical states of these perovskite catalysts. Because the interface features play a key role on heterogeneous catalysis. XPS survey spectra shown in Fig. S2 reflect the presence of La, Co, Fe and O elements

according to specific peaks around corresponding binding energy (BE). La cations present two doublets at 830 ~ 860 eV with satellite peaks, which are assigned to spin-orbital splitting of $\text{La } 3d_{3/2}$ and $3d_{5/2}$ [51]. The ignorable shift of La 3d peaks indicate the main changes of chemical states appear on B-site TMs and oxygen anions. The XPS spectra of O 1s for samples are displayed in Fig. 4b, emerging distinguishable energy distribution. The O 1s peaks generally could be deconvoluted into four typical peaks located at 528.6, 529.7, 531.2 and 533.2 eV, which are attributed to lattice oxygen, oxygen deficiencies/species and adsorbed oxygen-containing molecule, respectively [52,53]. The proportions of these oxygen species could be compared according to their peak area. LaCoO_3 (41.54 %) has the highest ratio of lattice oxygen, which is in accordance with its lowest V_O concentration. And, $\text{LaCo}_{0.95}\text{Fe}_{0.05}\text{O}_3$ (27.93 %) also presents larger amount of lattice oxygen than LaFeO_3 (16.8 %). Considering the highest EPR signal intensity in $\text{LaCo}_{0.95}\text{Fe}_{0.05}\text{O}_3$, it suggests that abundant V_O exist in mixed perovskite bulk instead of catalyst surface.

As shown in Fig. 4c, Fe 2p spectrum of LaFeO_3 has two specific peaks at about 710.1 and 723.5 eV, which are associated with Fe $2p_{3/2}$ and $2p_{1/2}$ orbitals [54]. Correspondingly, only a wide Fe 2p peak is observed for $\text{LaCo}_{0.95}\text{Fe}_{0.05}\text{O}_3$, which might result from its little substituted ratio and energy loss of photoelectron transition. Nevertheless, the bonding energy of Fe cations in $\text{LaCo}_{0.95}\text{Fe}_{0.05}\text{O}_3$ show obvious left shift to higher values, indicating that iron sites serve as electron donors. Moreover, Co 2p spectra displayed in Fig. 4d are split into two main spin doublets for Co $2p_{3/2}$ and $2p_{1/2}$ orbital peaks [55]. The Co $2p_{3/2}$ peak at 779.63 eV and $2p_{1/2}$ peak at 794.63 eV are assigned to Co^{3+} , with the energy splitting about 15 eV. As a contrast, Co $2p_{3/2}$ peak and $2p_{1/2}$ peak could be further deconvoluted for Co^{2+} cations at 781.12 eV and 796.21 eV, along with satellite peaks at around 788.48 and 803.80 eV. Comparing to the absence of iron substitution, the ratio of low valence-state cobalt ions in $\text{LaCo}_{0.95}\text{Fe}_{0.05}\text{O}_3$ is increased. Then, K-edge X-ray absorption

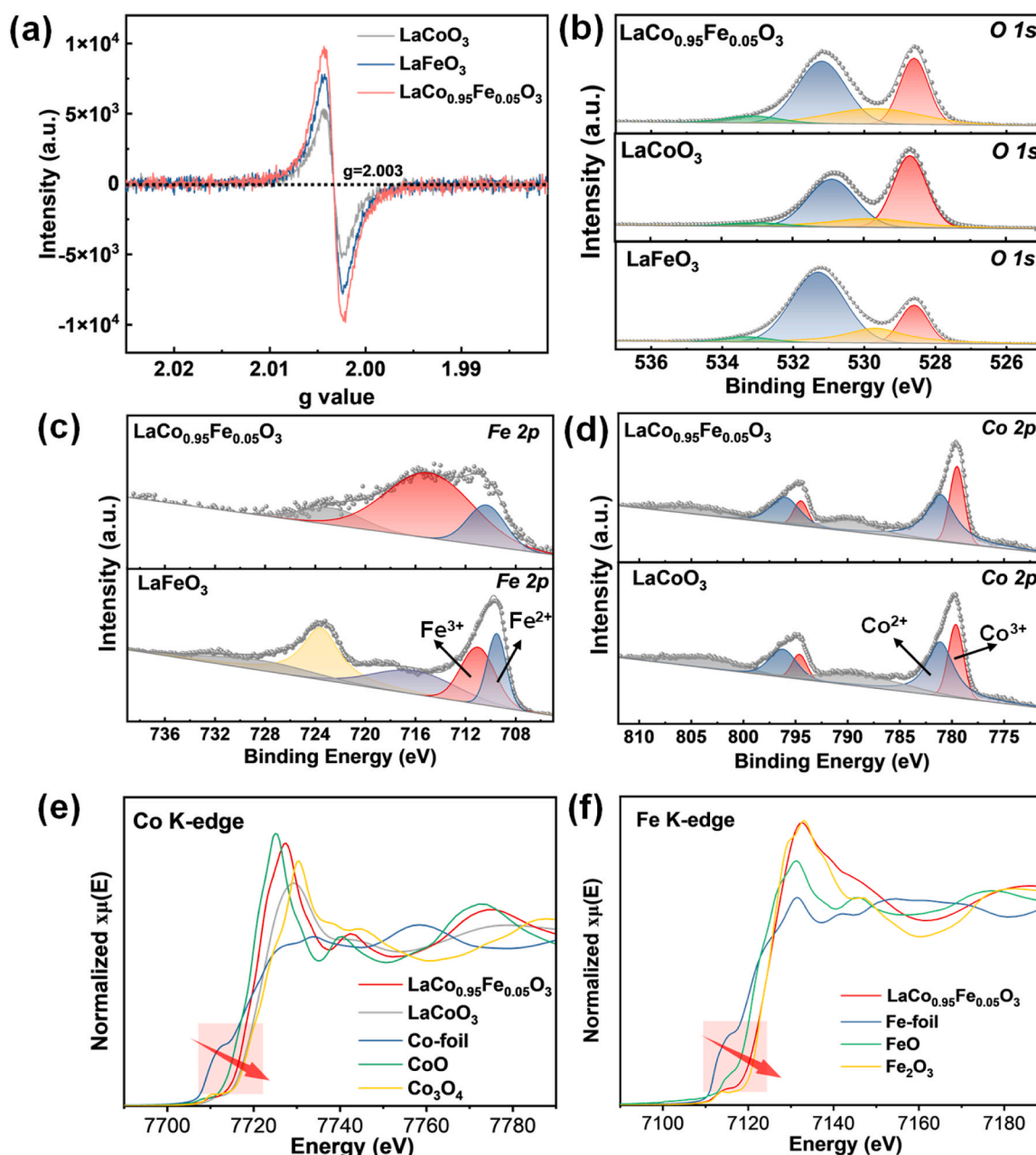


Fig. 4. EPR spectra (a), XPS peaks associated with O 1s (b), Fe 2p (c) and Co 2p (d) orbitals in LaCoO₃, LaCo_{0.95}Fe_{0.05}O₃ and LaFeO₃, and normalized Co (e), Fe (f) K-edge XANES of LaCo_{0.95}Fe_{0.05}O₃.

spectroscopy (XAS) was performed for B-site TM of LaCoO₃ and LaCo_{0.95}Fe_{0.05}O₃ to further identify their electronic status. As shown in Fig. 4e, X-ray absorption near edge structure (XANES) showed that the absorption edge position of Co K-edge of LaCo_{0.95}Fe_{0.05}O₃ was obviously larger than those of Co foil and CoO, while it was lower than that of LaCoO₃ or Co₃O₄. This position indicates cobalt cations have the valence status between +2 and +3. It also suggests that LaCo_{0.95}Fe_{0.05}O₃ has the lower valence-state Co ion comparing to LaCoO₃, owing the interaction with Fe substitution. On the other hand, the absorption edge position of Fe k-edge in Fig. 4f was far from Fe foil and FeO, which nearly approaches the position of Fe₂O₃. It means that valence state of substituted Fe cation is closer to +3 comparing with cobalt ones. The XAS results correspond to the XPS analysis, which indicates cobalt cation prefers to have enhanced electronic density by the electron donation from iron site. These spectroscopic features determine the enhanced electron exchange is achieved in Co-Fe cooperated LaCo_{0.95}Fe_{0.05}O₃ perovskite.

3.4. Activation mechanism

It is of importance to identify the real reactive centers, though the TM cations and oxygen species are reported to have the capability to activate PMS on perovskites. The related model will be used for further experimental and theoretical simulation. Having the similar electronegativity to HSO₅⁻ in PMS, the specific anion SCN⁻ was used to recognize the direct reactive centers. It is because this complexant thiocyanate ion has been confirmed to coordinate with transition metals strongly [56,57]. As shown in Fig. 5a, the presence of SCN⁻ can remarkably hinder the IOH degradation on each perovskite. It indicates that B-site cations are the primary reactive sites, and d-band heterogeneous catalysis is responsible to activate PMS in this system. Then, the reaction rate of PMS consumption was measured to estimate the activity of TM species. As displayed in Fig. 5b, the time-dependent PMS concentration was determined by a modified iodometric titration. LaCoO₃

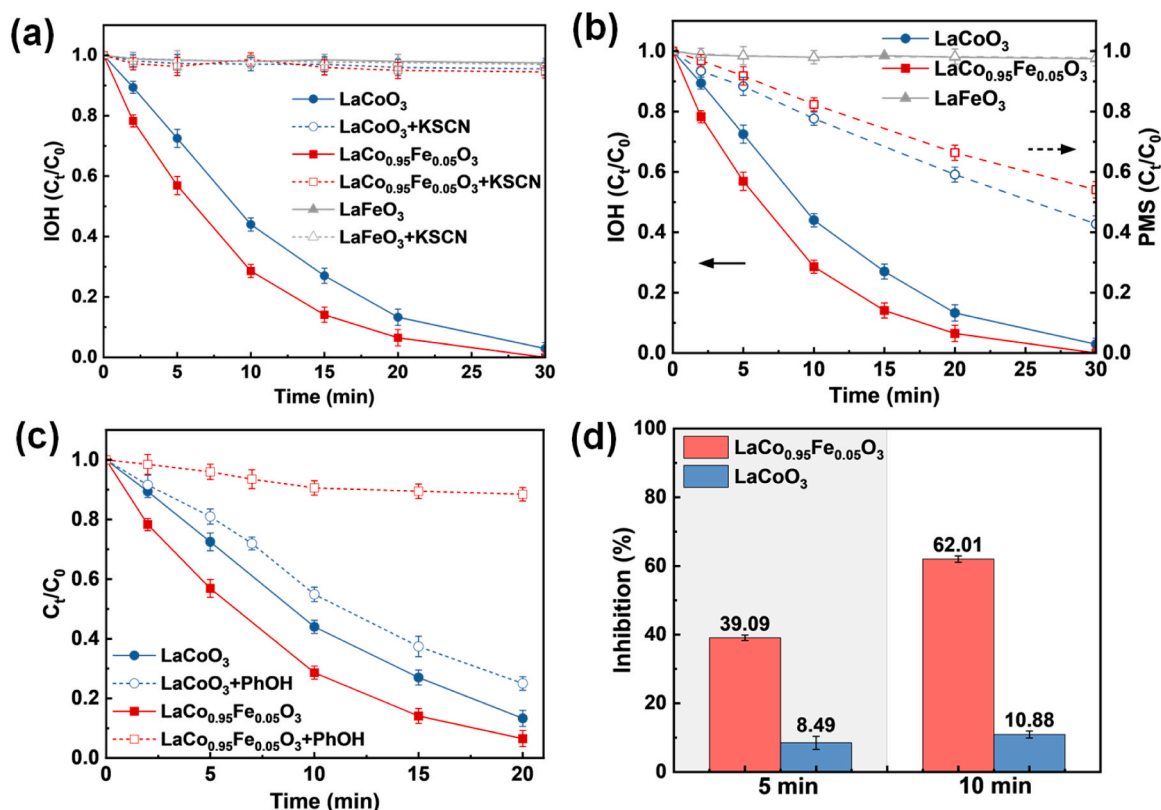


Fig. 5. Targeting passivation of TM sites for PMS activation on IOH removal (a), the relationship between IOH degradation and PMS consumption (b) inhibited effects of PhOH on IOH degradation (c) and kinetic rates (d) in perovskite/PMS system. Reaction conditions: [catalysts] = 50 mg L⁻¹, [PMS] = 0.1 mM, [IOH concentration] = 10 mg L⁻¹, [KSCN] = 0.1 mM, [PhOH] = 0.05 mM.

has the faster rate and larger proportion than LaCo_{0.95}Fe_{0.05}O₃ for PMS decomposition, though it has inferior activity to remove contaminant. It means that LaCo_{0.95}Fe_{0.05}O₃ contributes to better utilization rate of PMS-based active species. On the contrary, LaFeO₃ exhibits little PMS consumption, which is thus excluded for the following ROS detection.

The interfacial features of active species are crucial to the degrading performance of PMS consumption. The phenol (PhOH) thus was employed to detect the surface-bound species during persulfate-based oxidation [58]. As shown in Fig. 5c, PhOH exhibited significant inhibitory function to LaCo_{0.95}Fe_{0.05}O₃ comparing with LaCoO₃, which implies the important role of surface-bound ROS. And, the dosage effect of PhOH on IOH removal is illustrated in Fig. S3. The degrading performance of LaCo_{0.95}Fe_{0.05}O₃ would be reduced obviously when the PhOH concentration was increased from 0.01 to 0.1 mM, while LaCoO₃ did not suffer from the similar huge hinderance. It means that LaCo_{0.95}Fe_{0.05}O₃ is more sensitive to the change of phenol concentration. This situation suggests more surface-bound species located on LaCo_{0.95}Fe_{0.05}O₃. Besides, KI was also employed, because it has been reported as another quencher reacting with surface-bound radicals [59]. As shown in Fig. S4, the presence of KI brings about slighter inhibitory to LaCoO₃ than LaCo_{0.95}Fe_{0.05}O₃ towards IOH degradation, which confirms that LaCo_{0.95}Fe_{0.05}O₃ facilitates to generate surface-bound radicals. Considering the importance of triggering activation at the early stage, the detailed decontamination inhibition was inspected at the first 5 and 10 min. As displayed in Fig. 5d, LaCo_{0.95}Fe_{0.05}O₃ is more sensitive to be suppressed comparing to LaCoO₃. This indicates that the presence of iron cations facilitates the formation of surface-bound ROS on perovskites, prolonging the lifetime of active species. It is consistent with recent reports that Fe-based catalysts are beneficial to the preliminary persulfate activation [60]. In addition, the inhibitory efficiency of LaCoO₃ is always over half in contrast to LaCo_{0.95}Fe_{0.05}O₃, which suggests the cobalt cations still play the leading role on interfacial ROS.

The predominant ROS was distinguished by quenching experiments, which is beneficial to survey the activation mechanism on different catalysts. Common radical and non-radical scavengers including ethanol (EtOH), Tert-butanol (TBA), para-benzoquinone (p-BQ) and L-histidine (L-his) were employed to evaluate the contributions of various ROS [61–64]. The active species can be selectively quenched by EtOH, TBA, BQ and L-his, as EtOH containing α-H has high reaction rates with both SO₄^{•-} ($1.6 \times 10^7 \sim 7.7 \times 10^7 \text{ M}^{-1} \text{ s}^{-1}$) and •OH ($1.2 \times 10^9 \sim 2.8 \times 10^9 \text{ M}^{-1} \text{ s}^{-1}$). The absence of α-H hinders ability of TBA for scavenging SO₄^{•-} ($4.0 \times 10^5 \sim 9.5 \times 10^5 \text{ M}^{-1} \text{ s}^{-1}$), comparing to its superior reaction with •OH ($3.8 \times 10^9 \sim 7.6 \times 10^9 \text{ M}^{-1} \text{ s}^{-1}$). In addition, p-BQ is used to scavenge O₂^{•-} ($9.0 \times 10^8 \sim 1.0 \times 10^9 \text{ M}^{-1} \text{ s}^{-1}$), and L-his is widely used as an effective quencher of ¹O₂ ($3.1 \times 10^{10} \text{ M}^{-1} \text{ s}^{-1}$). As displayed in Fig. S5a–d, a series of quenching agents with different concentrations are chosen in the preliminary experiments to verify the reactive species for a suitable concentration. Consequently, we selected appropriate quencher dosages of 500 mM EtOH, 100 mM TBA, 10 mM p-BQ and 50 mM L-his for the following tests. LaCoO₃ and LaCo_{0.95}Fe_{0.05}O₃ exhibit similar quenching behaviors in Fig. 6a, where IOH degradation was almost completely inhibited with the addition of EtOH or L-his. And, the addition of TBA and p-BQ had a slight inhibitory effect on the degradation performance. The inhibited effects of these scavengers indicate the predominant function of SO₄^{•-} and ¹O₂. Then, the intermediate ROS were further surveyed by EPR spectra using spin-trapping agents shown in Fig. 6b–d and S6 [65]. The 1:2:2:1 four splitting lines are assigned to DMPO-•OH adducts (α_N = α_H = 14.9 G). LaCo_{0.95}Fe_{0.05}O₃ has stronger signals than LaCoO₃ for its advantageous generation of •OH, though •OH did not act as predominant ROS in these perovskite/PMS systems. Meanwhile, the characteristic peaks of spin adduct DMPO-SO₄^{•-} (hyperfine splitting constants of a_N = 13.2 G, a_H = 9.6 G, a_H = 1.48 G and a_H = 0.78 G) with six lines were observed, which suggests more generation of SO₄^{•-} by LaCo_{0.95}Fe_{0.05}O₃. And, DMPO-O₂^{•-} spin

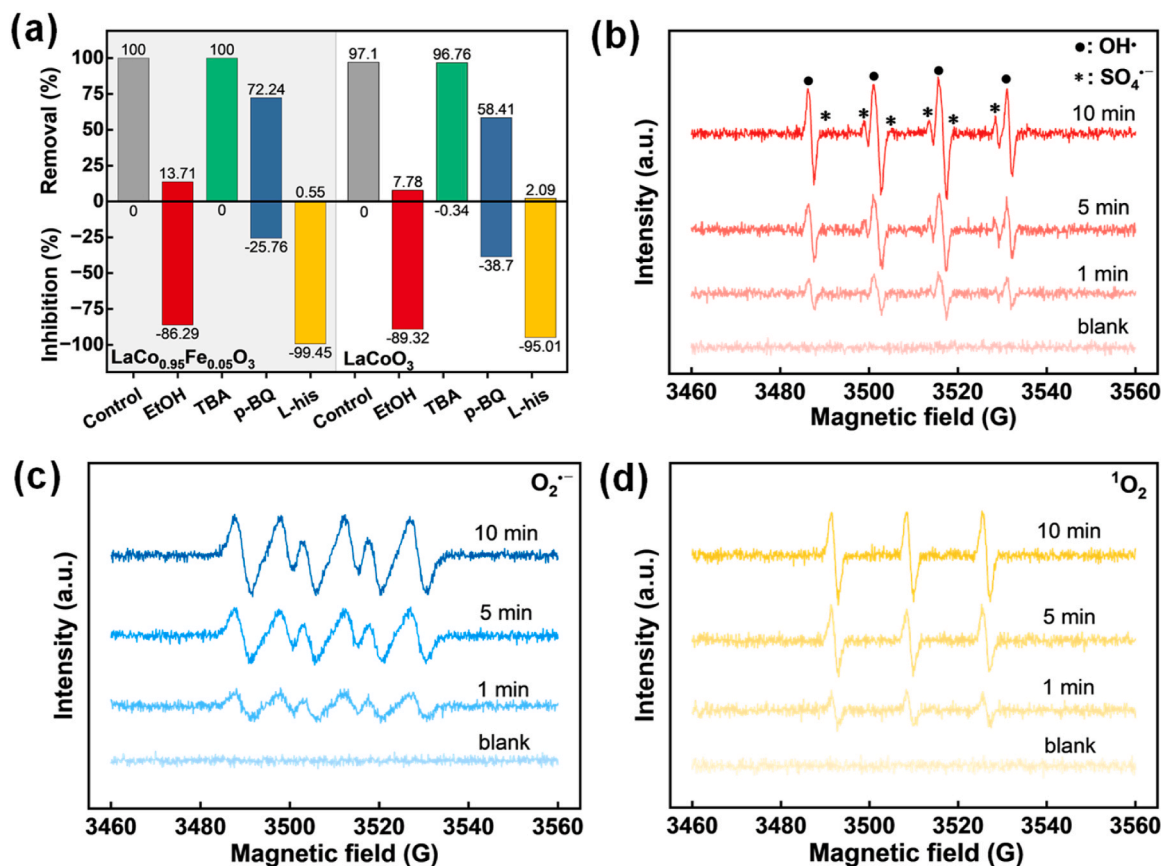


Fig. 6. Inhibitory rates of radical and nonradical scavengers (a) and corresponding spin-trapping EPR spectra of $\bullet\text{OH}$ and $\text{SO}_4^{\bullet-}$ (b), $\text{O}_2^{\bullet-}$ (c) and $^1\text{O}_2$ (d) in $\text{LaCo}_{0.95}\text{Fe}_{0.05}\text{O}_3/\text{PMS}$ system.

adduct with the intense four-line in Fig. 6c reveals the product of $\text{O}_2^{\bullet-}$ [66], while triplet signals of 1:1:1 splitting line in Fig. 6d, confirm the generation of $^1\text{O}_2$ [67]. These EPR spectra indicate that $\text{LaCo}_{0.95}\text{Fe}_{0.05}\text{O}_3$ has the superior activity to decompose PMS to generate active species.

3.5. Electrochemical analysis

Interfacial arrangements of energy bands of catalysts have a thermodynamic influence on the charge transfer among catalyst, PMS and contaminant, which regulates the barrier height of perovskite-solution junction. The surface reconstruction generally occurs on heterogeneous catalysts after cycling reaction for several times [68]. Then, the

cobalt-based oxygen-containing species e.g. (oxy)hydroxide would be formed, which have the semiconductor feature. As a consequence, the relational Fermi level position of catalyst immersed into contaminant solution could be inferred. Mott-Schottky tests were carried out to understand this thermodynamic factor on PMS activation, where the Fermi level is associated with the flat band potential (E_{FB}) [69]. As shown Fig. 7a, Mott-Schottky plots were extracted from impedance results, complying the Mott-Schottky equation.

$$\frac{1}{C^2} = \frac{2}{\epsilon\epsilon_0 e N_D} (E - E_{\text{FB}} - \frac{k_B T}{e}) \quad (1)$$

Where C is the capacitance, e is the elementary charge, ϵ and ϵ_0 are

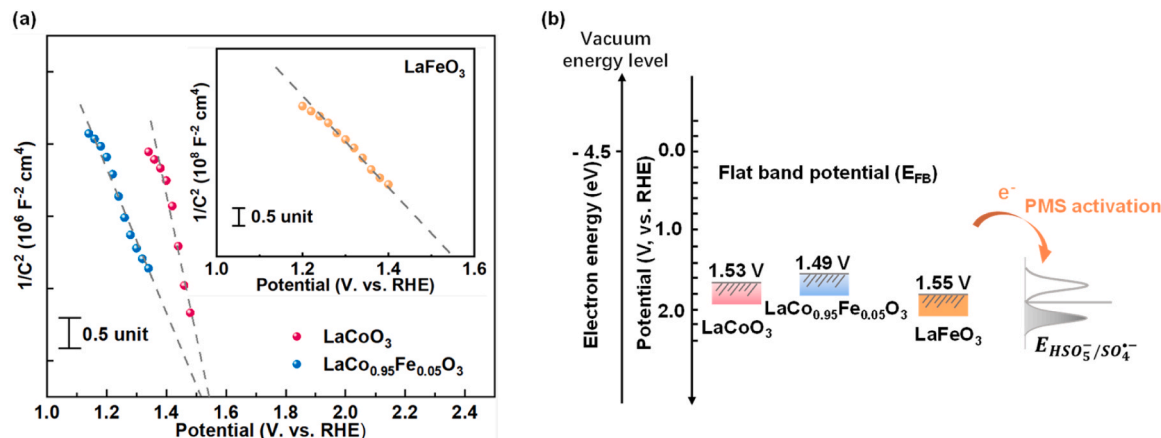


Fig. 7. Mott-Schottky measurements (a) and flat band potential (b) of perovskites. The frequency was fixed at 1 kHz.

dielectric coefficient, N_D is density of charge carrier, k_B is Boltzmann constant and T is the Kelvin temperature. It should be noted that the perovskite particles were adhered on glassy carbon as working electrode, and this rough structure might cause certain deviation from flat capacitor for ideal Mott-Schottky test. Nevertheless, the related potential-dependent change of surface capacitance still could reflect the Fermi level and surface properties of perovskite catalysts. The corresponding flat band potentials were calculated by the intercept. The E_{FB} of LaCoO_3 and LaFeO_3 is 1.53 and 1.55 V, respectively. Unlike these single TM perovskites, $\text{LaCo}_{0.95}\text{Fe}_{0.05}\text{O}_3$ has a lower E_{FB} of 1.49 V for higher position of Fermi level. As illustrated in Fig. 7b, down-bend Schottky barrier owing to p-type feature would be reduced with lifted E_{FB} . It promotes the electron exchange between adsorbed species and catalyst. The more negative flat band potential of catalyst is probably attributed to enriched oxygen defects, which leads to decreased ratio of O 2p electrons for energetic hybridization. And, $\text{LaCo}_{0.95}\text{Fe}_{0.05}\text{O}_3$ also owns more charge carriers in space charge region (depletion layer), which is indicated by its lower slope of Mott-Schottky plot according to Eq. (1). These advantages indicate that partial substitution of iron cations might have diminished barrier height to exchange electron with PMS activation. The activity trend and redox behaviors are consistent with this thermodynamically facilitated electron injection and acceptance on catalyst interface.

Electrochemical techniques provide an effective route to survey the physicochemical properties at catalyst interface, and were further performed to study kinetic features. Typical cyclic voltammetry (CV) was performed in the neutral and alkaline solution containing PMS and target contaminant [70]. The catalyst ink was loaded on glassy carbon-rotating disk electrode (GC-RDE), preventing the limitation of mass transfer. As displayed in Fig. S7, the TM cations generally reveal specific redox behaviors in alkaline condition, where obvious anodic and cathodic peaks at about 1.2 ~ 1.4 V stem from TM redox process. And, $\text{LaCo}_{0.95}\text{Fe}_{0.05}\text{O}_3$ always presents higher current density than LaCoO_3 at low bias potential, though its water oxidation is slightly inferior at potential over 1.5 V. Meanwhile, half-wave potential (i.e. $(E_a + E_c)/2$) of TM redox pairs can be calculated from CV curves, where

E_a and E_c are responding to anodic and cathodic potentials. $\text{LaCo}_{0.95}\text{Fe}_{0.05}\text{O}_3$ (1.35 V) exhibits a lower half-wave potential comparing with LaCoO_3 (1.40 V). It probably originates from the charge donation by Fe sites, because $\text{Fe}^{3+}/\text{Fe}^{2+}$ pairs have a more negative reversible potential than $\text{Co}^{3+}/\text{Co}^{2+}$ pairs. And, the gap of redox potentials for catalysts would be narrowed by oxygen vacancies whether PMS was present or not. These results further indicate Fe substitution could boost the conversion of $\text{Co}^{2+}/\text{Co}^{3+}/\text{Co}^{4+}$ species, promoting PMS activation.

As shown in Fig. 8a, the addition of PMS enhanced the cathodic peaks for each sample, which suggests that the reduction of Co^{3+} to Co^{2+} is facilitated, which is usually thought as a difficult step for PMS activation. Moreover, the responding potential of $\text{LaCo}_{0.95}\text{Fe}_{0.05}\text{O}_3$ and LaCoO_3 were shifted left over 100 mV, while LaFeO_3 revealed little change. It accounts for the easier reaction between cobalt ions and PMS, hindering their electrochemical reduction. Furthermore, the electrochemically active surface area (ECSA) is measured to evaluate inherent activity of active sites, which can be inferred from the double-layer capacitance (CDL) [71,72]. According to nearly rectangular CV curves shown in Fig. S8, the C_{DL} was calculated by scan-rate-dependent current density, which is fitted for the slope shown in Fig. 8b. And, $\text{LaCo}_{0.95}\text{Fe}_{0.05}\text{O}_3$ (0.411 mF cm^{-2}) has larger C_{DL} than LaCoO_3 (0.364 mF cm^{-2}) and LaFeO_3 (0.274 mF cm^{-2}), indicating its highest ECSA and more active sites.

Interfacial charge transfer on perovskites were further in-situ survey by electrochemical impedance spectroscopy (EIS). The frequency range was selected at 0.01 Hz to 100 kHz. The bias potentials were operated at 1.5 ~ 1.8 V according to CV behaviors of TM ions. As illustrated in Fig. 8c-f, Nyquist plots of samples were collected in the electrolyte containing PMS and contaminant. The typical Randles circuit was used to describe the charge-transfer processes, which is made up of the series resistance (R_s), the charge transfer resistance (R_{ct}) and capacitance (C_{CE}) at the catalyst-solution interface [73]. In EIS plots, the obvious semi-circle is originated from the parallel connection of R_{ct} and C_{CE} . At high bias potential (> 1.5 V), the semicircle appears in the high-frequency region, indicating the occurrence of charge transfer at catalyst-electrolyte interface. The smaller equivalent radius of the

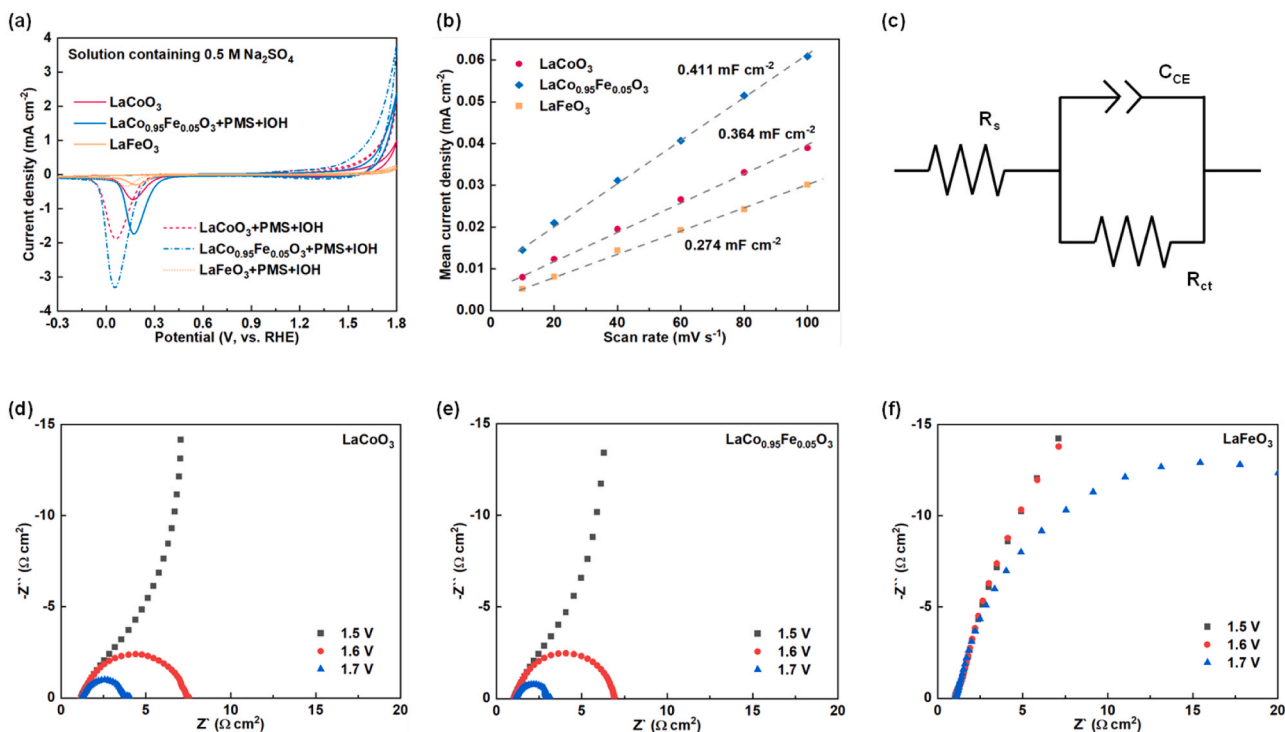


Fig. 8. CV curves (a), electrochemical active surface area (b), Randles circuit (c) and EIS Nyquist plots (d-f) of perovskites in contaminant solution containing 0.5 M Na_2SO_4 , 10 mg L^{-1} IOH with 0.1 mM PMS.

semicircle is assigned to the lower charge transfer resistance. Therefore, $\text{LaCo}_{0.95}\text{Fe}_{0.05}\text{O}_3$ exhibits greater advantage to exchange electron with reactants, since it always has smaller semicircle radius at each bias potential comparing with LaCoO_3 .

3.6. Theoretical calculations

The lattice distortion induced by Fe substitution have a powerful impact on TM d-orbital configurations affecting catalytic activity [74]. Thus, the electronic structures of Co, Fe and O were calculated by DFT. As shown in Fig. S9, the total DOS of $\text{LaCo}_{0.95}\text{Fe}_{0.05}\text{O}_3$ with/without fixing lattice parameters present insignificant difference, which suggests the certain lattice distortion contributes to strain tolerance. Then, electronic density of states (DOS) of perovskite catalysts were calculated in Fig. S10 to give the orbital-level insight. The dd-orbital PDOS possess a superior proportion on TM DOS for each sample, illustrating the pivotal role of d orbital electrons on catalytic activity. And, the partial density of states (PDOS) of Co-3d, Fe-3d and O-2p orbitals depicted in Fig. 9 were employed to survey their orbital hybridization for electron exchange. More attention should be paid on the PDOS in the near-Fermi-level energy region, because this region represents the reactive region of the oxide catalyst. For the absence of Fe ions, LaCoO_3 exhibits the finite overlap between Co 3d_{yz} and O 2p_z orbitals, most of whose PDOS are localized far lower from the Fermi level of perovskite. On the contrary, the major energy states of Co 3d and O 2p reveal increased density in $\text{LaCo}_{0.95}\text{Fe}_{0.05}\text{O}_3$ with partial Fe replacement. And, the relational band centers were shifted right towards Fermi level enhancing the Co-O covalence. These changes might be caused by the lattice distortion converting the orbital orientation of TM and oxygen species. Consequently, it illustrates the larger overlap of Co 3d and O 2p orbitals than LaCoO_3 around the Fermi level, facilitating charge transfer. The Fe 3d-PDOS also reveal certain overlap with Co 3d energy states, which is possibly built by the superexchange among TM cations via oxygen anions and deficiencies. This result also agrees with the varied chemical states of TM in XPS spectra.

3.7. Structure induced superexchange interaction

According to above experiments and theoretical simulation, the partial substitution of Fe ions in octahedral B sites of perovskites is assumed to arise lattice mismatch and oxygen defects, changing the orientation of TM 3d and O 2p for overlap of orbital electron cloud [75]. Consequently, the electronic structure is regulated for different

performance of PMS activation. To confirm this hypothesis, the tolerance factor (t) of each sample was calculated to investigate the relationship between lattice distortion and catalytic activity. As shown in Fig. 10a, the tolerance factors of all $\text{LaCo}_{1-x}\text{Fe}_x\text{O}_3$ are not in the range between 0.7 and 0.9, which means their cubic structure instead of orthorhombic or rhombohedral perovskite. It suggests that the t factor should be not too close nor too far from the ideal value, where the moderated lattice distortion contributes to superior activity. The nearly volcano-relationship is partially attributed to the different electro-negativity and galvanic oxidation between Co and Fe cations. The corresponding mechanism is schemed in Fig. 10b. The standard potentials of $\text{Fe}^{3+}/\text{Fe}^{2+}$ and $\text{Co}^{3+}/\text{Co}^{2+}$ redox pairs are about 0.77 and 1.81 V, respectively. It means cobalt cations have a lower d-band to accept electron. And, the oxygen deficiencies promote the relaxation of electrons localized by oxygen anions, uplifting the band of O 2p. Then, iron ions prefer to donate electron to cobalt sites across the superexchange with oxygen species, increasing the Fermi level. As a consequence, it facilitated the charge transfer with PMS. It means the moderate Fe substitution could optimize the bulk and interface electronic structures of $\text{LaCo}_{1-x}\text{Fe}_x\text{O}_3$ perovskite, then the PMS activation is promoted thermodynamically and kinetically for improved contaminant degradation.

3.8. Performance and degradation pathways

To further investigate reaction mechanism and practical effects on the contaminant degradation, different environmental conditions were carried out for $\text{LaCo}_{0.95}\text{Fe}_{0.05}\text{O}_3$. This perovskite/PMS is somewhat sensitive to pH changes in Fig. 11a, which suggests the lattice oxygen is an important species participating the activation. And, the typical anions were added because active species in PMS (HSO_5^-) presents the negative feature in aqueous environment. As shown in Fig. 11b, SO_4^{2-} and NO_3^- anions generally existed in industrial wastewater exhibit insignificant impedance on IOH removal. On the contrary, the Cl^- ions lead to visible inhibition, as the residual IOH concentration was over 70 %. It is possibly originated from that Cl^- could reduce $\bullet\text{OH}$ and $\text{SO}_4^{\bullet-}$ into chlorine species (e.g. $\text{ClOH}^{\bullet-}$, $\text{Cl}_2^{\bullet-}$ and $\bullet\text{Cl}$) with decreased redox potential [76]. The HCO_3^- also prevents the degradation process, because it could bind with catalyst's surface and compete with contaminant for radical consumption [77].

In addition, this catalyst can be employed to remove other contaminants, such as sulfamethoxazole (SMX) and bisphenol A (BPA), besides IOH. The similar kinetic plots shown in Fig. 11c indicate that the contaminant removal mainly depends on the activity of catalyst to

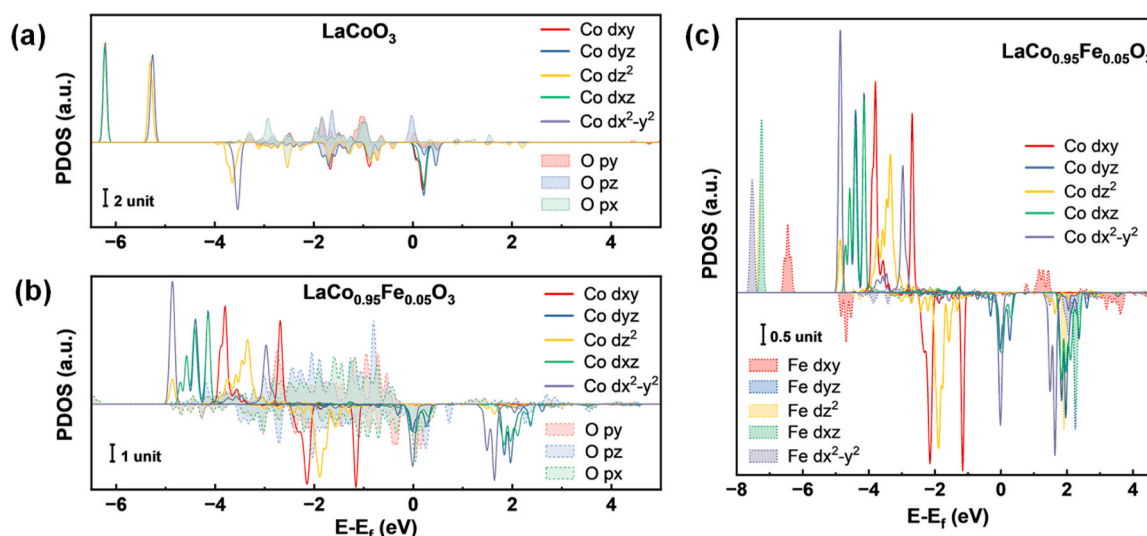


Fig. 9. PDOS of Co-3d, Fe-3d and O-2p orbitals on LaCoO_3 (a) and $\text{LaCo}_{0.95}\text{Fe}_{0.05}\text{O}_3$ (b, c).

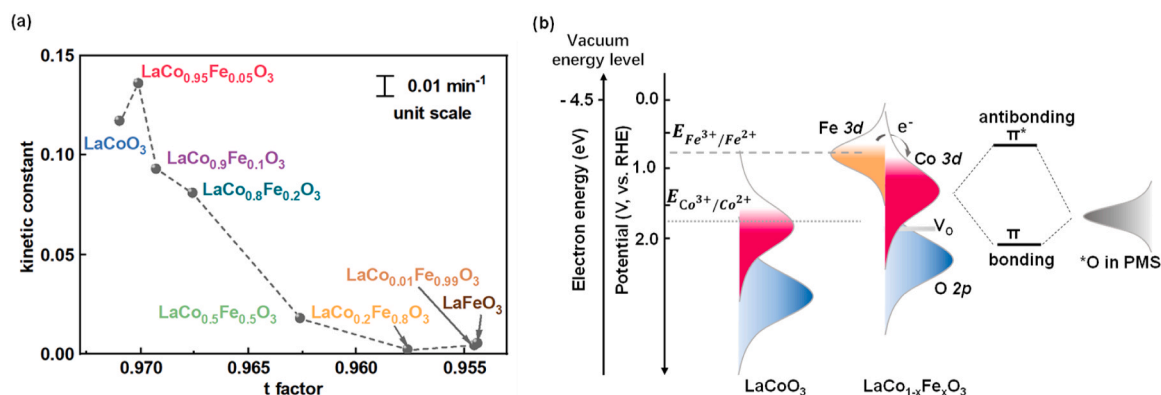


Fig. 10. The lattice distortion dependent contaminant degradation (a), and related mechanic scheme (b) of mixed LaCo_{1-x}Fe_xO₃ perovskite via PMS activation.

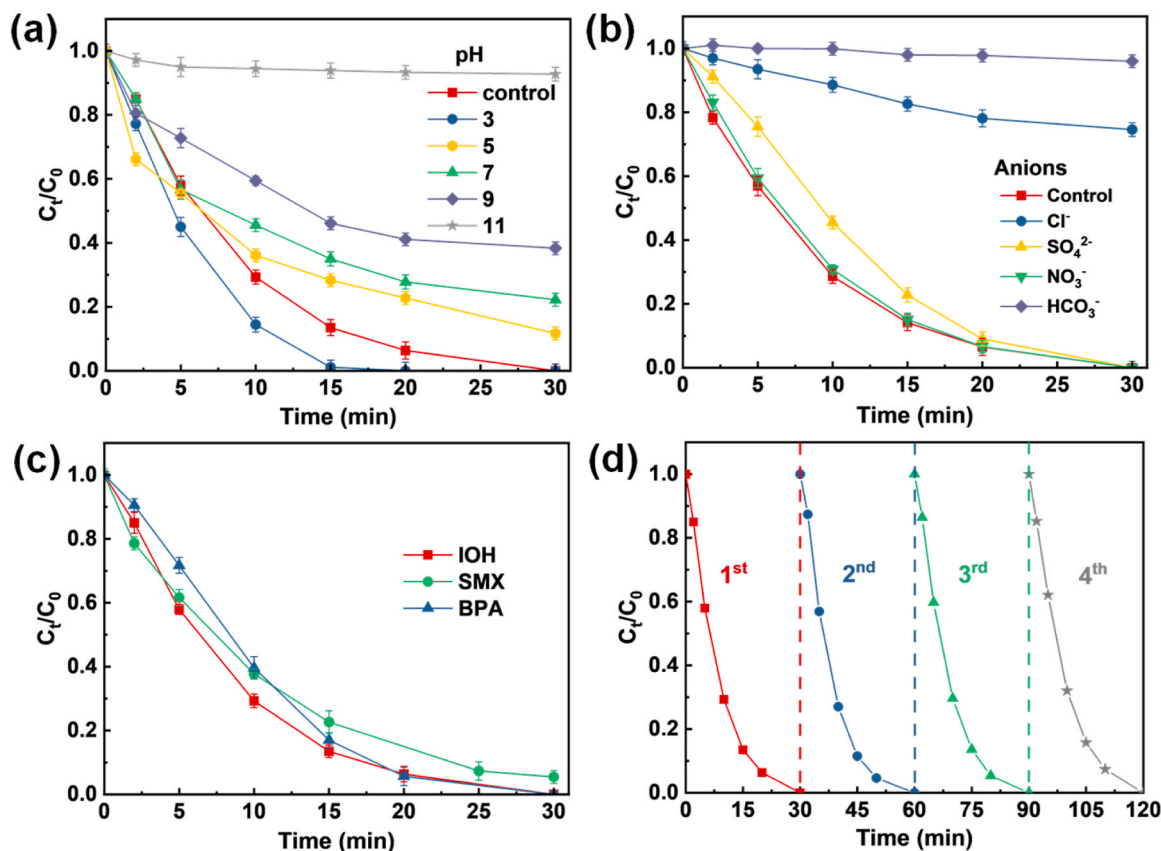


Fig. 11. Different influencing factors in LaCo_{0.95}Fe_{0.05}O₃/PMS system: pH (a); anions (b); pollutants (c); cycling runs (d).

activate PMS. The XPS spectra presented in Fig. S11 were further collected after IOH degradation. The O 1s spectra indicate that more adsorbed oxygen species were generated on LaCo_{0.95}Fe_{0.05}O₃ after contaminant degradation. It probably results from the reason that surface reconstruction enriched partial intermediate oxygen species, which suggests that LaCo_{0.95}Fe_{0.05}O₃ facilitates interfacial transformation for heterogeneous catalysis. And, the cobalt cations exhibit certain change, while the proportion of Fe³⁺ was increased about 1.36 %. These results indicate the electron donation of iron cations through superexchange interaction and stable cycling transformation of cobalt redox pairs during PMS activation. Moreover, the stability test was investigated by cycling experiments as shown in Fig. 11d. The removal rate of IOH could still reach 100 % after several cycling experiments, and the leaching of cobalt and iron ions are 80 and 49 μg L⁻¹, respectively. These results indicate its good cycling performance and reusability.

Finally, the degradation pathways of IOH contamination were analyzed by LC-MS. As presented in Fig. S12 and Table. S2, and intermediate products were detected. Based on the corresponding *m/z* values and previous reports [78,79], six possible transformation pathways were proposed as shown in Fig. 12. The organic substance IOH is degraded to small molecules mainly through six pathways. In pathway I, IOH is degraded to P2 by amide hydrolysis, deiodination, •OH attack and C-OH oxidation process. And, IOH can be degraded to P5 in pathway II by amide hydrolysis and deiodination reactions. Pathway III includes amide hydrolysis, hydrogen abstraction and deiodination, and then IOH is degraded to P9. Meanwhile, pathways IV and V illustrate that contaminant could be degraded to P13 and P17 by amide hydrolysis, amine oxidation, hydrogen abstraction and deiodinations. Moreover, IOH also could be degraded in Pathway VI, including amide hydrolysis, amino oxidation, deiodination, -OH attack, and C-OH oxidation

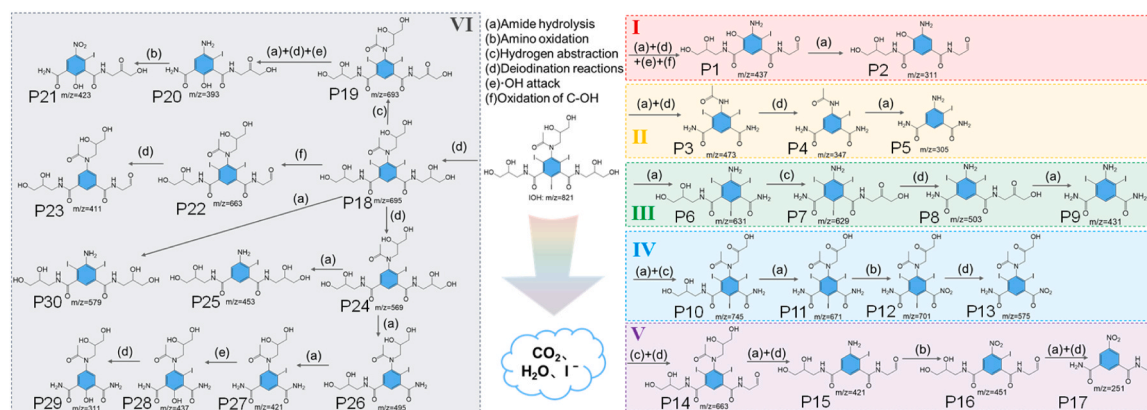


Fig. 12. Proposed IOH degradation pathways.

obtaining the products P21, P23, P29, and P30. Consequently, these substances would be further degraded to small molecules including CO₂, H₂O and I⁻. In addition, the toxicity of intermediates was surveyed in the LaCo_{0.95}Fe_{0.05}O₃/PMS oxidizing systems. The toxicity estimation software tool (T.E.S.T) based on quantitative structure-activity relationship (QSAR) was used to calculate the Fathead minnow LC₅₀ (96 hr) and Oral rat LD₅₀. From the predicted toxicity results illustrated in Fig. S13 and S14, some of the intermediates are still toxic, but they will be mineralized as the degradation reaction proceeds. Therefore, the intermediates will progressively become low toxic after a period of degradation in this Fenton-like system.

4. Conclusion

The various Fe substitutions were performed to modulate the octahedral CoO₆ units in LaCo_{1-x}Fe_xO₃ perovskites, and the LaCo_{0.95}Fe_{0.05}O₃/PMS system presents superior IOH degradation. The reactive centers suffer from certain lattice distortion because of the radii mismatch of Co and Fe cations. Then, the enriched oxygen defects were constructed in the perovskite bulk besides on the surface. Targeted passivation reveals that B-site cobalt cations serve as the main active sites, while Fe ions promote the electron compensation. And the predominant ROS are SO₄^{•-} and ¹O₂. According to the mediates of these oxygen species, the superexchanges were built among TM ions for fast charge transport. Systemic spectroscopic and electrochemical measurements reveal that cobalt and iron sites prefer to accept and donate electrons, respectively. The certain Fe substitution would reduce the barrier height of LaCo_{1-x}Fe_xO₃ to activate PMS, and facilitates valence exchange of cation redox pairs with feasible electron transfer at catalyst-solution interface. These thermodynamic and kinetic promotions are further confirmed by theoretical simulation, illustrating the improved electronic structures. In addition, tolerance factor is demonstrated as an important descriptor to evaluate the structure dependent performance for contaminant degradation. Our work provides a new mechanistic insight to synergistic catalysis for improving persulfate-based catalysis.

CRediT authorship contribution statement

Yijie Wu: data curation, writing - original draft. **Tiantian She:** data curation. **Yunheng Wang:** data curation. **Zhe Xu:** conceptualization, data curation, investigation; methodology, funding acquisition, writing - review & Editing. **Tao Huang:** data curation. **Qiuyi Ji:** investigation. **Haiou Song:** resources. **Shaogui Yang:** resources. **Shiyan Li:** resources. **Shicheng Yan:** supervision, resources. **Limin Zhang:** resources. **Huan He:** supervision, project administration, funding acquisition.

Declaration of Competing Interest

The authors declare that they have no potential competing financial interests or personal relationships that could have appeared to influence the work reported in this paper.

Data Availability

Data will be made available on request.

Acknowledgements

This research was supported by National Natural Science Foundation of China (No. 52002187, 21777067 and 51908293), the Qing Lan Project of Jiangsu Province and the Six Talent Peaks Project in Jiangsu Province (No. JNHB-059), China Postdoctoral Science Foundation (2023M731739), Jiangsu Funding Program for Excellent Postdoctoral Talent (No. 2022ZB352).

Appendix A. Supporting information

Supplementary data associated with this article can be found in the online version at doi:10.1016/j.apcatb.2023.123569.

References

- [1] J. Lee, U. Von Gunten, J. Kim, Persulfate-based advanced oxidation: critical assessment of opportunities and roadblocks, *Environ. Sci. Technol.* 54 (2020) 3064–3081, <https://doi.org/10.1021/acs.est.9b07082>.
- [2] M.J. Huang, Y.S. Li, C.Q. Zhang, C. Cui, Q.Q. Huang, M.K. Li, Z.M. Qiang, T. Zhou, X.H. Wu, H.Q. Yu, Facilely tuning the intrinsic catalytic sites of the spinel oxide for peroxymonosulfate activation: From fundamental investigation to pilot-scale demonstration, *Proc. Natl. Acad. Sci. U. S. A.* 119 (2022), e2202682119, <https://doi.org/10.1073/pnas.2202682119>.
- [3] W. Ren, C. Cheng, P.H. Shao, X.B. Luo, H. Zhang, S.B. Wang, X.G. Duan, Origins of electron-transfer regime in persulfate-based nonradical oxidation processes, *Environ. Sci. Technol.* 56 (2022) 78–97, <https://doi.org/10.1021/acs.est.1c05374>.
- [4] J.J. Qi, X.Y. Yang, P.Y. Pan, T.B. Huang, X.D. Yang, C.C. Wang, W. Liu, Interface engineering of Co(OH)₂ nanosheets growing on the KNO₃ perovskite based on electronic structure modulation for enhanced peroxymonosulfate activation, *Environ. Sci. Technol.* 56 (2022) 5200–5212, <https://doi.org/10.1021/acs.est.1c08806>.
- [5] L.D. Lai, Y.L. He, H.Y. Zhou, B.K. Huang, G. Yao, B. Lai, Critical review of natural iron-based minerals used as heterogeneous catalysts in peroxide activation processes: Characteristics, applications and mechanisms, *J. Hazard. Mater.* 416 (2021), 125809, <https://doi.org/10.1016/j.jhazmat.2021.125809>.
- [6] X.N. Li, X. Huang, S.B. Xi, S. Miao, J. Ding, W.Z. Cai, S. Liu, X.L. Yang, H.B. Yang, J. Gao, J.H. Wang, Y.Q. Huang, T. Zhang, B. Liu, Single cobalt atoms anchored on porous N-doped graphene with dual reaction sites for efficient Fenton-like catalysis, *J. Am. Chem. Soc.* 140 (2018) 12469–12475, <https://doi.org/10.1021/jacs.8b05992>.
- [7] J. Miao, Y. Zhu, J.Y. Lang, J.Z. Zhang, S.X. Cheng, B.X. Zhou, L.Z. Zhang, P.J. J. Alvarez, M.C. Long, Spin-state-dependent peroxymonosulfate activation of single-atom M–N moieties via a radical-free pathway, *ACS Catal.* 11 (2021) 9569–9577, <https://doi.org/10.1021/acscatal.1c02031>.

- [8] P.D. Hu, M.C. Long, Cobalt-catalyzed sulfate radical-based advanced oxidation: a review on heterogeneous catalysts and applications, *Appl. Catal. B: Environ.* 181 (2016) 103–117, <https://doi.org/10.1016/j.apcatb.2015.07.024>.
- [9] L. An, C. Wei, M. Lu, H.W. Liu, Y.B. Chen, G.G. Scherer, A.C. Fisher, P.X. Xi, Z.C. J. Xu, C.H. Yan, Recent development of oxygen evolution electrocatalysts in acidic environment, *Adv. Mater.* 33 (2021), 2006328, <https://doi.org/10.1002/adma.202006328>.
- [10] Z. Xu, Y.J. Wu, Q.Y. Ji, T.Z. Li, C.M. Xu, C.D. Qi, H. He, S.G. Yang, S.Y. Li, S.C. Yan, C. Sun, L.M. Zhang, Z.G. Zou, Understanding spatial effects of tetrahedral and octahedral cobalt cations on peroxymonosulfate activation for efficient pollution degradation, *Appl. Catal. B: Environ.* 291 (2021), 120072, <https://doi.org/10.1016/j.apcatb.2021.120072>.
- [11] X.G. Duan, C. Su, J. Miao, Y.J. Zhong, Z.P. Shao, S.B. Wang, H.Q. Sun, Insights into perovskite-catalyzed peroxymonosulfate activation: Maneuverable cobalt sites for promoted evolution of sulfate radicals, *Appl. Catal. B: Environ.* 220 (2018) 626–634, <https://doi.org/10.1016/j.apcatb.2017.08.088>.
- [12] S.B. Hammouda, F.P. Zhao, Z. Safaei, V. Srivastava, D. Lakshmi Ramasamy, S. Iftikhar, S. Kalliola, M. Sillanpää, Degradation and mineralization of phenol in aqueous medium by heterogeneous monopersulfate activation on nanostructuring cobalt based-perovskite catalysts $\text{A}(\text{CoO}_3)$ (A=La, Ba, Sr and Ce): Characterization, kinetics and mechanism study, *Appl. Catal. B: Environ.* 215 (2017) 60–73, <https://doi.org/10.1016/j.apcatb.2017.05.051>.
- [13] D.N. Mueller, M.L. Machala, H. Blum, W.C. Chueh, Redox activity of surface oxygen anions in oxygen-deficient perovskite oxides during electrochemical reactions, *Nat. Commun.* 6 (2015), 6097, <https://doi.org/10.1038/ncomms7097>.
- [14] O.P. Taran, A.B. Ayusheev, O.L. Ogorodnikova, I.P. Prosvirnin, L.A. Isupova, V. N. Parmon, Perovskite-like catalysts LaBO_3 (B=Cu, Fe, Mn, Co, Ni) for wet peroxide oxidation of phenol, *Appl. Catal. B: Environ.* 180 (2016) 86–93, <https://doi.org/10.1016/j.apcatb.2015.05.055>.
- [15] K.A. Lin, Y.C. Chen, Y.F. Lin, LaMO_3 perovskites (M=Co, Cu, Fe and Ni) as heterogeneous catalysts for activating peroxymonosulfate in water, *Chem. Eng. Sci.* 160 (2017) 96–105, <https://doi.org/10.1016/j.ces.2016.11.017>.
- [16] X.M. Li, M.R. Li, X. Ma, J. Miao, R. Ran, W. Zhou, S.B. Wang, Z.P. Shao, Nonstoichiometric perovskite for enhanced catalytic oxidation through excess A-site cation, *Chem. Eng. Sci.* 219 (2020), 115596, <https://doi.org/10.1016/j.ces.2020.115596>.
- [17] P. Liang, D.D. Meng, Y. Liang, Z. Wang, C. Zhang, S.B. Wang, Z.H. Zhang, Cation deficiency tuned $\text{LaCoO}_{3-\delta}$ perovskite for peroxymonosulfate activation towards bisphenol A degradation, *Chem. Eng. J.* 409 (2021), 128196, <https://doi.org/10.1016/j.cej.2020.128196>.
- [18] B.H. Niu, L.H. Wang, M.Z. Li, W.L. Yao, K. Zang, L. Zhou, X.W. Hu, Y.A. Zheng, Lattice B-doping evolved ferromagnetic perovskite-like catalyst for enhancing persulfate-based degradation of norfloxacin, *J. Hazard. Mater.* 425 (2022), 127949, <https://doi.org/10.1016/j.jhazmat.2021.127949>.
- [19] Q.N. Yang, X.Y. Niu, Y.J. Zhu, Y. Cui, Y. Chao, P. Liang, C. Zhang, S.B. Wang, Modulating anion defect in $\text{La}_{0.6}\text{Sr}_{0.4}\text{Co}_{0.8}\text{Fe}_{0.2}\text{O}_{3-\delta}$ for enhanced catalytic performance on peroxymonosulfate activation: Importance of hydrated electrons and metal-oxygen covalency, *J. Hazard. Mater.* 432 (2022), 128686, <https://doi.org/10.1016/j.jhazmat.2022.128686>.
- [20] Y.F. Rao, Y.F. Zhang, F.M. Han, H.C. Guo, Y. Huang, R.Y. Li, F. Qi, J. Ma, Heterogeneous activation of peroxymonosulfate by LaFeO_3 for diclofenac degradation: DFT-assisted mechanistic study and degradation pathways, *Chem. Eng. J.* 352 (2018) 601–611, <https://doi.org/10.1016/j.cej.2018.07.062>.
- [21] C. Su, X.G. Duan, J. Miao, Y.J. Zhong, W. Zhou, S.B. Wang, Z.P. Shao, Mixed conducting perovskite materials as superior catalysts for fast aqueous-phase advanced oxidation: a mechanistic study, *ACS Catal.* 7 (2017) 388–397, <https://doi.org/10.1021/acscatal.6b02303>.
- [22] W.X. Wang, Y. Liu, Y.F. Yue, H.H. Wang, G. Cheng, C.Y. Gao, C.L. Chen, Y.J. Ai, Z. Chen, X.K. Wang, The confined interlayer growth of ultrathin two-dimensional Fe_3O_4 nanosheets with enriched oxygen vacancies for peroxymonosulfate activation, *ACS Catal.* 11 (2021) 11256–11265, <https://doi.org/10.1021/acscatal.1c03331>.
- [23] Z. Xu, Y.J. Wu, X. Wang, Q.Y. Ji, T.Z. Li, H. He, H.O. Song, S.G. Yang, S.Y. Li, S. C. Yan, L.M. Zhang, Z.G. Zou, Identifying the role of oxygen vacancy on cobalt-based perovskites towards peroxymonosulfate activation for efficient iohexol degradation, *Appl. Catal. B: Environ.* 319 (2022), 121901, <https://doi.org/10.1016/j.apcatb.2022.121901>.
- [24] D. Yu, J.H. He, T.P. Xie, Q. Xu, Q.X. Zhu, J. Yang, J.B. An, F. Ye, J.K. Wang, B. Xiang, New insights into Sr-O bonds enhances Co/Fe catalytic activity in SrCoFe perovskite for boosted peroxymonosulfate activation, *Chem. Eng. J.* 426 (2021), 131525, <https://doi.org/10.1016/j.cej.2021.131525>.
- [25] A. Vojvodic, J.K. Nørskov, Optimizing perovskites for the water-splitting reaction, *Science* 334 (2011) 1355–1356, <https://www.science.org/doi/abs/10.1126/science.1215081>.
- [26] S. Lu, G.L. Wang, S. Chen, H.T. Yu, F. Ye, X. Quan, Heterogeneous activation of peroxymonosulfate by $\text{LaCo}_{1-x}\text{Cu}_x\text{O}_3$ perovskites for degradation of organic pollutants, *J. Hazard. Mater.* 353 (2018) 401–409, <https://doi.org/10.1016/j.jhazmat.2018.04.021>.
- [27] J. Miao, J. Sunarso, X.G. Duan, W. Zhou, S.B. Wang, Z.P. Shao, Nanostructured Co-Mn containing perovskites for degradation of pollutants: Insight into the activity and stability, *J. Hazard. Mater.* 349 (2018) 177–185, <https://doi.org/10.1016/j.jhazmat.2018.01.054>.
- [28] Y.X. Wang, Z.X. Chi, C.M. Chen, C. Su, D.Q. Liu, Y. Liu, X.G. Duan, S.B. Wang, Facet- and defect-dependent activity of perovskites in catalytic evolution of sulfate radicals, *Appl. Catal. B: Environ.* 272 (2020), 118972, <https://doi.org/10.1016/j.apcatb.2020.118972>.
- [29] L. Yang, Y. Jiao, X.M. Xu, Y.L. Pan, C. Su, X.G. Duan, H.Q. Sun, S.M. Liu, S.B. Wang, Z.P. Shao, Superstructures with atomic-level arranged perovskite and oxide layers for advanced oxidation with an enhanced non-free radical pathway, *ACS Sustain. Chem. Eng.* 10 (2022) 1899–1909, <https://doi.org/10.1021/acssuschemeng.1c07605>.
- [30] L.F. Zhang, Y.Q. Zhang, J.H. Wei, W. Liu, Perovskite $\text{LaFe}_x\text{Co}_{1-x}\text{O}_{3-\delta}$ deposited SiO_2 catalytic membrane for deeply cleaning wastewater, *Chem. Eng. J.* 403 (2021), 126386, <https://doi.org/10.1016/j.cej.2020.126386>.
- [31] J.N. Jing, X.C. Wang, M.H. Zhou, Electro-enhanced activation of peroxymonosulfate by a novel perovskite- TiO_2 composite anode with ultra-high efficiency and low energy consumption: The generation and dominant role of singlet oxygen, *Water Res.* 232 (2023), 119682, <https://doi.org/10.1016/j.watres.2023.119682>.
- [32] H. Zhang, R.J. Zhang, Z.C. Wu, F.S. Yang, M.F. Luo, G. Yao, Z.M. Ao, B. Lai, Cobalt-doped boosted the peroxymonosulfate activation performance of LaFeO_3 perovskite for atrazine degradation, *Chem. Eng. J.* 452 (2023), 139427, <https://doi.org/10.1016/j.cej.2022.139427>.
- [33] A. Margellou, D. Manos, D. Petrakis, I. Konstantinou, Activation of persulfate by $\text{LaFe}_{1-x}\text{Co}_x\text{O}_3$ perovskite catalysts for the degradation of phenolics: Effect of synthetic method and metal substitution, *Sci. Total Environ.* 832 (2022), 155063, <https://doi.org/10.1016/j.scitotenv.2022.155063>.
- [34] J.M. Byrne, V.S. Coker, E. Cespedes, P.L. Wincott, D.J. Vaughan, R. a D. Patrick, G. Van Der Laan, E. Arenholz, F. Tuna, M. Bencsik, J.R. Lloyd, N.D. Telling, Biosynthesis of zinc substituted magnetite nanoparticles with enhanced magnetic properties, *Adv. Funct. Mater.* 24 (2014) 2518–2529, <https://doi.org/10.1002/adfm.201303230>.
- [35] K. Wang, C. Han, F.P. Li, Y. Liu, Z.P. Shao, L.H. Liu, S.B. Wang, S.M. Liu, An intrinsic descriptor of perovskite cobaltites for catalytic peroxymonosulfate activation toward water remediation, *Appl. Catal. B: Environ.* 320 (2023), 121990, <https://doi.org/10.1016/j.apcatb.2022.121990>.
- [36] M. Zhu, J. Miao, X.G. Duan, D.Q. Guan, Y.J. Zhong, S.B. Wang, W. Zhou, Z.P. Shao, Postsynthesis growth of CoOOH nanostructure on $\text{SrCo}_{0.6}\text{Ti}_{0.4}\text{O}_{3-\delta}$ perovskite surface for enhanced degradation of aqueous organic contaminants, *ACS Sustain. Chem. Eng.* 6 (2018) 15737–15748, <https://doi.org/10.1021/acssuschemeng.8b04289>.
- [37] G. Mamba, P.J. Mafa, V. Muthuraj, A. Mashayekh-Salehi, S. Royer, T.I. T. Nkambule, S. Rtimi, Heterogeneous advanced oxidation processes over stoichiometric ABO_3 perovskite nanostructures, *Mater. Today Nano* 18 (2022), 100184, <https://doi.org/10.1016/j.mtnano.2022.100184>.
- [38] P.P. Zhang, Y.Y. Yang, X.G. Duan, Y.J. Liu, S.B. Wang, Density functional theory calculations for insight into the heterocatalyst reactivity and mechanism in persulfate-based advanced oxidation reactions, *ACS Catal.* 11 (2021) 11129–11159, <https://doi.org/10.1021/acscatal.1c03099>.
- [39] G. Kresse, D. Joubert, From ultrasoft pseudopotentials to the projector augmented-wave method, *Phys. Rev. B* 59 (1999) 1758–1775, <https://link.aps.org/doi/10.1103/PhysRevB.59.1758>.
- [40] J.P. Perdew, K. Burke, M. Ernzerhof, Generalized gradient approximation made simple, *Phys. Rev. Lett.* 77 (1996) 3865–3868, <https://link.aps.org/doi/10.1103/PhysRevLett.77.3865>.
- [41] F. Maldonado, A. Stashans, DFT study of Ag and La codoped BaTiO_3 , *J. Phys. Chem. Solids* 102 (2017) 136–141, <https://doi.org/10.1016/j.jpcs.2016.11.016>.
- [42] J.M. Munro, K. Latimer, M.K. Horton, S. Dwaraknath, K.A. Persson, An improved symmetry-based approach to reciprocal space path selection in band structure calculations, *NPJ Comput. Mater.* 6 (2020), 112, <https://doi.org/10.1038/s41524-020-00383-7>.
- [43] Y. Zhou, S.N. Sun, S.B. Xi, Y. Duan, T. Sritharan, Y.H. Du, Z.C.J. Xu, Superexchange effects on oxygen reduction activity of edge-sharing $[\text{Co}_6\text{Mn}_{1-x}\text{O}_6]$ octahedra in spinel oxide, *Adv. Mater.* 30 (2018), 1705407, <https://doi.org/10.1002/adma.201705407>.
- [44] J.B. Goodenough, P.M. Raccach, Complex vs band formation in perovskite oxides, *J. Appl. Phys.* 36 (2004) 1031–1032, <https://doi.org/10.1063/1.1714087>.
- [45] R.D. Shannon, Revised effective ionic radii and systematic studies of interatomic distances in halides and chalcogenides, *Acta Cryst. A* 32 (1976) 751–767, <https://doi.org/10.1107/S0567739476001551>.
- [46] P. Joshi, M. Saleem, S. Tiwari, J. Shukla, A. Mishra, Diffraction data analysis, microstructure and dielectric studies of transition metal doped LaCoO_3 , *Mater. Today: Proc.* 54 (2022) 890–894, <https://doi.org/10.1016/j.matpr.2021.11.206>.
- [47] C. Cheng, S.W. Gao, J.C. Zhu, G.Y. Wang, L.J. Wang, X.F. Xia, Enhanced performance of LaFeO_3 perovskite for peroxymonosulfate activation through strontium doping towards 2,4-D degradation, *Chem. Eng. J.* 384 (2020), <https://doi.org/10.1016/j.cej.2019.123377>.
- [48] D. Kubba, I. Ahmed, P. Kour, R. Biswas, H. Kaur, K. Yadav, K.K. Haldar, LaCoO_3 perovskite nanoparticles embedded in NiCo_2O_4 nanoflowers as electrocatalysts for oxygen evolution, *ACS Appl. Nano Mater.* 5 (2022) 16344–16353, <https://doi.org/10.1021/acsaanm.2c03395>.
- [49] C. Feng, Q.Q. Gao, G.Y. Xiong, Y.F. Chen, Y. Pan, Z.Y. Fei, Y.P. Li, Y.K. Lu, C.G. Liu, Y.Q. Liu, Defect engineering technique for the fabrication of LaCoO_3 perovskite catalyst via urea treatment for total oxidation of propane, *Appl. Catal. B: Environ.* 304 (2022), 121005, <https://doi.org/10.1016/j.apcatb.2021.121005>.
- [50] K. Wang, C. Han, Z.P. Shao, J.S. Qiu, S.B. Wang, S.M. Liu, Perovskite oxide catalysts for advanced oxidation reactions, *Adv. Funct. Mater.* 31 (2021), 2102089, <https://doi.org/10.1002/adfm.202102089>.
- [51] T.X. Nguyen, Y.C. Liao, C.C. Lin, Y.H. Su, J.M. Ting, Advanced high entropy perovskite oxide electrocatalyst for oxygen evolution reaction, *Adv. Funct. Mater.* 31 (2021), 2101632, <https://doi.org/10.1002/adfm.202101632>.

- [52] Y.G. Wang, J.W. Ren, Y.Q. Wang, F.Y. Zhang, X.H. Liu, Y. Guo, G.Z. Lu, Nanocasted synthesis of mesoporous LaCoO_3 perovskite with extremely high surface area and excellent activity in methane combustion, *J. Phys. Chem. C* 112 (2008) 15293–15298, <https://doi.org/10.1021/jp8048394>.
- [53] K.A. Stoerzinger, W.T. Hong, E.J. Crumlin, H. Bluhm, M.D. Biegalski, Y. Shao-Horn, Water reactivity on the LaCoO_3 (001) surface: an ambient pressure X-ray photoelectron spectroscopy study, *J. Phys. Chem. C* 118 (2014) 19733–19741, <https://doi.org/10.1021/jp502970r>.
- [54] Z.M. Lu, H. Zhou, B. Qian, S. Wang, Y.F. Zheng, L. Ge, H. Chen, Y. and Fe co-doped LaNiO_3 perovskite as a novel bifunctional electrocatalyst for rechargeable zinc-air batteries, *Int. J. Hydrog. Energy* 48 (2023) 8082–8092, <https://doi.org/10.1016/j.ijhydene.2022.11.228>.
- [55] X.H. Zheng, B. Li, L.J. Shen, Y.N. Cao, Y.Y. Zhan, S.T. Zheng, S.P. Wang, L.L. Jiang, Oxygen vacancies engineering of Fe doped LaCoO_3 perovskite catalysts for efficient H_2S selective oxidation, *Appl. Catal. B: Environ.* 329 (2023), 122526, <https://doi.org/10.1016/j.apcatb.2023.122526>.
- [56] M.S. Thorum, J.M. Hankett, A.A. Gewirth, Poisoning the oxygen reduction reaction on carbon-supported Fe and Cu electrocatalysts: evidence for metal-centered activity, *J. Phys. Chem. Lett.* 2 (2011) 295–298, <https://doi.org/10.1021/jz1016284>.
- [57] Z. Xu, W.C. Li, Y.D. Yan, H.X. Wang, H. Zhu, M.M. Zhao, S.C. Yan, Z.G. Zou, In-situ formed hydroxide accelerating water dissociation kinetics on Co_3N for hydrogen production in alkaline solution, *ACS Appl. Mater. Interfaces* 10 (2018) 22102–22109, <https://doi.org/10.1021/acsami.8b04596>.
- [58] Z.Y. Bai, S.S. Gao, H.R. Yu, X.W. Liu, J.Y. Tian, Layered metal oxides loaded ceramic membrane activating peroxymonosulfate for mitigation of NOM membrane fouling, *Water Res.* 222 (2022), 118928, <https://doi.org/10.1016/j.watres.2022.118928>.
- [59] C.Q. Zhu, F.Q. Liu, C. Ling, H. Jiang, H.D. Wu, A.M. Li, Growth of graphene-supported hollow cobalt sulfide nanocrystals via MOF-templated ligand exchange as surface-bound radical sinks for highly efficient bisphenol A degradation, *Appl. Catal. B: Environ.* 242 (2019) 238–248, <https://doi.org/10.1016/j.apcatb.2018.09.088>.
- [60] H.Y. Dong, Q.H. Xu, L.S. Lian, Y. Li, S.C. Wang, C. Li, X.H. Guan, Degradation of organic contaminants in the Fe(II) /peroxymonosulfate process under acidic conditions: the overlooked rapid oxidation stage, *Environ. Sci. Technol.* 55 (2021) 15390–15399, <https://doi.org/10.1021/acs.est.1c04563>.
- [61] C.Y. Zhu, F.X. Zhu, D.D. Dionysiou, D.M. Zhou, G.D. Fang, J. Gao, Contribution of alcohol radicals to contaminant degradation in quenching studies of persulfate activation process, *Water Res.* 139 (2018) 66–73, <https://doi.org/10.1016/j.watres.2018.03.069>.
- [62] X. Guo, Q.C. Zhang, H.W. He, A. Cai, S.B. Xi, J.Q. Du, F.B. Zhang, X.B. Fan, W. C. Peng, Y. Li, Wastewater flocculation substrate derived three-dimensional ordered macroporous Co single-atom catalyst for singlet oxygen-dominated peroxymonosulfate activation, *Appl. Catal. B: Environ.* 335 (2023), 122886, <https://doi.org/10.1016/j.apcatb.2023.122886>.
- [63] Y. Guo, Y.X. Zhang, G. Yu, Y.J. Wang, Revisiting the role of reactive oxygen species for pollutant abatement during catalytic ozonation: the probe approach versus the scavenger approach, *Appl. Catal. B: Environ.* 280 (2021), 119418, <https://doi.org/10.1016/j.apcatb.2020.119418>.
- [64] J.P. Liang, L. Fu, K. Gao, X.G. Duan, Accelerating radical generation from peroxymonosulfate by confined variable Co species toward ciprofloxacin mineralization: ROS quantification and mechanisms elucidation, *Appl. Catal. B: Environ.* 315 (2022), 121542, <https://doi.org/10.1016/j.apcatb.2022.121542>.
- [65] Z.S. Wei, F.A. Villamena, L.K. Weavers, Kinetics and mechanism of ultrasonic activation of persulfate: an in situ EPR spin trapping study, *Environ. Sci. Technol.* 51 (2017) 3410–3417, <https://doi.org/10.1021/acs.est.6b05392>.
- [66] H.N. Che, X. Gao, J. Chen, J. Hou, Y.H. Ao, P.F. Wang, Iodide-Induced fragmentation of polymerized hydrophilic carbon nitride for high-performance quasi-homogeneous photocatalytic H_2O_2 production, *Angew. Chem. Int. Ed.* 60 (2021) 25546–25550, <https://doi.org/10.1002/anie.202111769>.
- [67] X.Y. Mi, P.F. Wang, S.Z. Xu, L. Su, H. Zhong, H.T. Wang, Y. Li, S.H. Zhan, Almost 100% peroxymonosulfate conversion to singlet oxygen on single-atom CoN_{2+2} sites, *Angew. Chem. Int. Ed.* 60 (2021) 4588–4593, <https://doi.org/10.1002/anie.202014472>.
- [68] C. Wu, X.P. Wang, Y. Tang, H.Y. Zhong, X. Zhang, A.Q. Zou, J.L. Zhu, C.Z. Diao, S. B. Xi, J.M. Xue, J.G. Wu, Origin of surface reconstruction in lattice oxygen oxidation mechanism based-transition metal oxides: a spontaneous chemical process, *Angew. Chem. Int. Ed.* 62 (2023), <https://doi.org/10.1002/anie.202218599>.
- [69] J.Q. Li, L.Y. Meng, J. Cheng, Thermodynamic conditions for the nernstian response of the flat band potential of the metal oxide semiconductor: A theoretical study, *J. Phys. Chem. C* 126 (2022) 578–587, <https://doi.org/10.1021/acs.jpcc.1c07625>.
- [70] H.Y. Li, Y.B. Chen, J.J. Ge, X.H. Liu, A.C. Fisher, M.P. Sherburne, J.W. Ager, Z. J. Xu, Active phase on $\text{SrCo}_{1-x}\text{Fe}_x\text{O}_{3-\delta}$ ($0 \leq x \leq 0.5$) perovskite for water oxidation: reconstructed surface versus remaining bulk, *J. Am. Chem. Soc.* 143 (2021) 108–115, <https://doi.org/10.1021/jacsau.0c00022>.
- [71] C.C.L. Mccrory, S.H. Jung, J.C. Peters, T.F. Jaramillo, Benchmarking heterogeneous electrocatalysts for the oxygen evolution reaction, *J. Am. Chem. Soc.* 135 (2013) 16977–16987, <https://doi.org/10.1021/ja407115p>.
- [72] Z. Xu, H.Y. Wang, Y.Z. Wen, W.C. Li, C.Y. Sun, Y.T. He, Z. Shi, L. Pei, Y.D. Chen, S. C. Yan, Z.G. Zou, Balancing catalytic activity and interface energetics of electrocatalyst-coated photoanodes for photoelectrochemical water splitting, *ACS Appl. Mater. Interfaces* 10 (2018) 3624–3633, <https://doi.org/10.1021/acsami.7b17348>.
- [73] Z. Xu, W.C. Li, X.H. Wang, B. Wang, Z. Shi, C. Dong, S.C. Yan, Z.G. Zou, Novel cobalt germanium hydroxide for electrochemical water oxidation, *ACS Appl. Mater. Interfaces* 10 (2018) 30357–30366, <https://doi.org/10.1021/acsami.8b09247>.
- [74] Y. Duan, S.N. Sun, S.B. Xi, X. Ren, Y. Zhou, G.L. Zhang, H.T. Yang, Y.H. Du, Z.C. J. Xu, Tailoring the Co 3d-O 2p covalency in LaCoO_3 by Fe substitution to promote oxygen evolution reaction, *Chem. Mater.* 29 (2017) 10534–10541, <https://doi.org/10.1021/acs.chemmater.7b04534>.
- [75] S.N. Sun, Y.M. Sun, Y. Zhou, S.B. Xi, X. Ren, B.C. Huang, H.B. Liao, L.P. Wang, Y. H. Du, Z.C.J. Xu, Shifting oxygen charge towards octahedral metal: a way to promote water oxidation on cobalt spinel oxides, *Angew. Chem. Int. Ed.* 58 (2019) 6042–6047, <https://doi.org/10.1002/anie.201902114>.
- [76] X.J. Lai, X.N. Ning, J.Y. Chen, Y. Li, Y.P. Zhang, Y.Q. Yuan, Comparison of the $\text{Fe}^{2+}/\text{H}_2\text{O}_2$ and $\text{Fe}^{2+}/\text{PMS}$ systems in simulated sludge: Removal of PAHs, migration of elements and formation of chlorination by-products, *J. Hazard. Mater.* 398 (2020), 122826, <https://doi.org/10.1016/j.jhazmat.2020.122826>.
- [77] G.B. Wen, B.H. Ren, Y. Zheng, M. Li, C. Silva, S.Q. Song, Z. Zhang, H.Z. Dou, L. Zhao, D. Luo, A.P. Yu, Z.W. Chen, Engineering electrochemical surface for efficient carbon dioxide upgrade, *Adv. Energy Mater.* 12 (2022), 2103289, <https://doi.org/10.1002/aenm.202103289>.
- [78] Q. Zhong, Y. Sun, C.M. Xu, Y.F. Li, D.Y. Sun, L.L. Wu, S.G. Yang, Y.Z. Liu, C.D. Qi, Z. Xu, H. He, S.Y. Li, Z.Y. Wang, S.B. Wang, $\text{Fe}_3\text{Se}_4/\text{C}$ superlattice nanocrystals for peroxymonosulfate activation: Intrinsic nature of Fe spin state, *Appl. Catal. B: Environ.* 339 (2023), 123113, <https://doi.org/10.1016/j.apcatb.2023.123113>.
- [79] C.Y. Hu, Y.Y. Zhu, B. Xu, T.Y. Zhang, Y.L. Lin, C. Xiong, Q.B. Wang, D.D. Huang, L. Xu, Fe_3O_4 catalytic ozonation of iohexol degradation in the presence of 1-hydroxybenzotriazole: Performance, transformation mechanism, and pathways, *Sep. Purif. Technol.* 289 (2022), 120810, <https://doi.org/10.1016/j.seppur.2022.120810>.